Implications of Shallow Water in Numerical Simulations of a Surface Effect Ship

David Geoffrey Lyons

Thesis submitted to the faculty of the Virginia Polytechnic Institute and State University in partial fulfillment of the requirements for the degree of

Master of Science
In
Ocean Engineering

Wayne L. Neu, Chair
Alan J. Brown
Leigh S. McCue-Weil

September 11, 2014
Blacksburg, VA

Keywords: SES, Overset Mesh, Shallow Water, Depth Froude Number

Implications of Shallow Water in Numerical Simulations of a Surface Effect Ship

David Geoffrey Lyons

ABSTRACT

Overset, or Chimera, meshes are used to discretize the governing equations within a computational domain using multiple meshes that overlap in an arbitrary manner. The overset meshing technique is most applicable to problems dealing with multiple or moving bodies. Deep water simulations were carried out using both single and overset grid techniques for the evaluation of the overset grid application. These simulations were carried out using the commercial CFD code STAR-CCM+ by CD-adapco. The geometry simulated is that of a SES model (T-Craft) tested at the Naval Surface Warfare Center Carderock Division. The craft is simulated with two degrees of freedom, allowing movement in heave and pitch in response to displacement of the free surface. Agreement between the single and overset grid techniques was deemed reasonable to extend to future shallow water cases. However, due to longer run times of the overset mesh, the traditional or single mesh technique should be employed whenever applicable. In order to extend existing full craft CFD simulations of a surface effect ship (SES) into shallow water and maneuvering cases, an overset mesh is needed. Simulations of the SES were performed and monitored at various depth Froude numbers resulting in subcritical, critical, and supercritical flow regimes. Resistance, pitch response, and free surface response of the SES were compared between the shallow water simulations. The SES produced wider wakes, perpendicular to the craft, at simulations closer to the critical flow regime. Critical flow occurs at a depth Froude number between 0.9 and 0.95. Progression of shallow water effects through the three flow regimes agrees well with shallow water theory.

TABLE OF CONTENTS

LIST OF FIGURES

LIST OF TABLES

NOMENCLATURE

R_w	Wavemaking Drag
C_w	Coefficient of Wavemaking Drag
p_c	Cushion Pressure
B_c	Cushion Width
ρ_w	Density of Water
g	Gravitational Acceleration
V_c	Velocity of Surface Waves
L_W	Length of Wave from Crest to Crest
h	Water Depth
ν	Kinematic Viscosity
F	External Body Force
U	Characteristic Velocity
δt	Time-step
δx	Local Grid Size
Fn_d	Depth Froude Number

ABBREVIATIONS

CFD	Computational Fluid Dynamics
CFL	Courant-Friedrichs-Lewy number
DOF	Degree of Freedom
HRIC	High Resolution Interface Capturing
NSWCCD	Naval Surface Warfare Center Carderock Division
SES	Surface Effect Ship
VOF	Volume of Fluid

1. INTRODUCTION

A surface effect ship (SES) consists of two catamaran hulls with flexible seals located in the bow and aft end used to enclose an air cushion. Fans are used to pump in air to the cushion, creating excess pressure that lifts the ship. The air cushion also creates a mean depression of the free surface that causes waves to develop underneath the craft. Numerical simulations were performed by Donnelly [1] to monitor the dynamics of a SES and visualize the complex free surface underneath the air cushion. Results presented in Donnelly were used to validate experimental data on an identical SES model at the Naval Surface Warfare Center, Carderock Division as part of the T-Craft program. Experimental results can be seen in Bishop [2]. This thesis contains comparisons of the same craft using a traditional meshing technique and an overset meshing technique.

The first simulation (or baseline simulation) dealt with the SES with a traditional meshing technique or without an overset mesh. The second simulation quantified the usefulness of the overset meshing technique by examining that same SES. The area of interest is comparing results of the free surface profiles and the forces/motions the SES undergoes with and without the overset meshing technique. Once the overset meshing technique was deemed practical, it was applied to the SES in a number of shallow water simulations. Ship resistance is sensitive to depth effects. Shallow water can drastically change the potential flow and wake patterns around a ship. The domain depth was altered for seven different depth Froude numbers. These seven domain depths were chosen to demonstrate the SES performance from subcritical regions through the critical change and into supercritical flow regions. With the help of computational fluid dynamics (CFD), the free surface can simply be visualized showing the progression of the wave systems as domain depth changes. Monitoring the free surface, therefore; the behavior of the bow and stern wave systems, can shed light to the behavior of the SES. A comparison of the motions and forces was done between each of the simulations to determine the effect of shallow water on the SES.

CFD is a powerful tool allowing for the dynamic behavior of physical systems to be visualized. CFD uses numerical methods to solve the nonlinear differential equations to the Navier-Stokes equations. Further discussion will neglect viscosity, therefore, only the Euler equations will be utilized. The Euler equations can be derived by removing these viscosity terms from the Navier-Stokes equations leaving only continuity and momentum. The computations of these Euler equations use the commercial CFD code, STAR-CCM+. Overset (also known as chimera) meshes allow for the use of multiple/separate meshes to be overlaid with each other. The advantages and disadvantages of the overset meshing technique will be discussed later in the report. For practicality of this overset meshing technique, two separate simulations of a SES were run.

1.1 RESISTANCE OF SES

The air cushion of the SES introduces an additional resistance component not seen by a typical catamaran. Like a catamaran, a SES has two rigid side-hulls but with the addition of forward and aft flexible seals to enclose an air cushion. Resistance components of a SES are composed of wavemaking drag due to the air cushion and side hulls, aerodynamic profile drag, seal drag, friction drag due to side hulls, appendage drag, hydrodynamic momentum drag, and drag due of the differential air momentum leakage between bow and stern seals. The main focus of this thesis will be to examine the wavemaking drag due to the effects of the air cushion, since all simulations neglected viscosity and the resistance is proportional to the mass density of the fluid. Air density is 1/1000 of water density. Excess pressure inside the air cushion leads to a mean depression of the free surface inside the hull relative to outside the hull. This contributes to the wave resistance. The waves generated by the air cushion are the largest source of the total wavemaking drag seen on the SES during calm water situations. Wavemaking drag due to the air cushion can be defined as:

$$R_w = C_w \left(\frac{{p_c}^2 B_c}{\rho_w g}\right) \tag{1}$$

where C_w is the wavemaking drag coefficient, p_c is the cushion pressure, B_c is the beam of the cushion, ρ_w is the density of water, g is the gravitational acceleration as seen in Yun and Bliault [3]. Wavemaking resistance is proportional to the length to beam ratio. SES's have a larger beam to length ratio than a traditional monohull vessel. As a result, interference effects become stronger between the bow and stern wave systems since the wave motion is more two dimensional. To reduce this in phase interference effect of the bow and stern wave systems and the resulting drag "hump" in the resistance curves, the length to beam ratio of the SES can be increased. Other factors that contribute to variation in wavemaking resistance seen by the craft are water depth, acceleration of the craft, and the orientation of the craft in relation to an incoming wave. Additional air cushion theory pertaining to the SES can be found in Donnelly [1] and Yun [3].

1.2 SHALLOW WATER EFFECTS

The depth of the water alters the potential flow around the hull of a ship. Restrictions in water depth lead to intensified resistance effects due to increased sinkage and trim that the ship experiences. This sinkage occurs in restricted depth or shallow water because the water beneath the hull must speed up which, in turn, results in a greater reduction of the pressure. Shallow water also varies the velocity at which the surface waves travel. In a given water depth, h, the velocity of the surface waves, V_c, travels with

$${V_c}^2 = \frac{g L_W}{2\pi} \tanh\left(\frac{2\pi h}{L_W}\right) \tag{2}$$

where L_W is length of the wave from crest to crest and g is gravity. In a deep water wave, h approaches infinity, therefore, the tanh term goes to one. The deep water wave velocity tends with

$$V_c{}^2 = \frac{gL_W}{2\pi} \tag{3}$$

As the water depth decreases, the tanh term now approaches $\frac{2\pi h}{L_W}$. The shallow water wave velocity can be approximated by

$$V_c{}^2 = gh \tag{4}$$

Equations 2-4 can be found in Lewis [4]. The wake pattern undergoes a transition from diverging waves with a convex line of advance and transverse waves in deep water to only diverging waves with a concave line of advance in shallow waters beyond the critical change. This wake pattern transition is due to the variation in wave speed previously discussed. The critical change occurs at the point where $V = \sqrt{gh}$. When the critical change is being approached, the ship produces a disturbance traveling at the same speed as itself. Therefore, the entirety of the wavemaking effect is produced in the crest and at angles normal to its direction of motion. These deviations in wake patterns based on water depth drastically affect the resistance of a ship. In shallow water, as the ship approaches the critical change or speed, the resistance of the ship will tend to increase rapidly. Speeds at which this occurs are considered subcritical. Once the ship surpasses the critical change, the resistance of the ship will continue to increase but at lower rate than in deep water. Therefore, the resistance will actually become less than in deep water. This can be attributed to a limit in wave energy generation forced by the shallow water. Speeds above the critical change are referred to as being supercritical found in Lewis[4].

2. T-CRAFT MODEL

The generic T-Craft was designed by John Hoyt III. Design features were derived from each of three (Alion, Umoe Mandal, and Textron Marine) contract hull designs. The Naval Surface Warfare Center Carderock Division (NSWCCD) built and tested this generic T-Craft model (model number 5887) in 2008 (Figure 1). The model features rigid side hulls with finger type bow and transverse seals and a double lobe type lobe seal seen in Figure 2. The three seals separate the air cushion into forward and aft sections. Two four inch blower fans, Jabsco Model 35400-0010, were equipped to the model to pressurize the air cushions. Ducts through the hull direct flow from the blower fans into the air cushions. Particulars of the model can be seen in Table 1. The computational model used was a simplistic variation of the aforementioned experimental model.

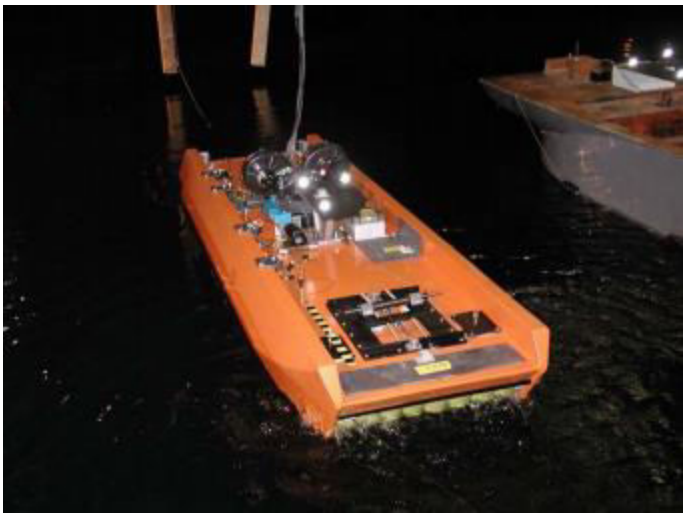

Figure 1: NSWCCD Model Number 5887, generic T-Craft model in Bishop [2].

Figure 2: Underside of T-Craft model with seals in Bishop [2].

Table 1: T-Craft Model Particulars taken from Bishop [2].

Linear Scale	1: 30.209
Length Overall	99.5 in, 2.5273 m
Length Waterline (off cushion)	98 in, 2.4892 m
Length Waterline (on cushion)	88 in, 2.352 m
Beam Max	29 in, 0.7366 m
Cushion Width	21.5 in, 0.5461 m
Cushion Length	87.5 in, 2.2225 m
Displacement	119 lbs FW, 54 kg – (121.5 lbs from report)
LCG, forward of wet deck transom	48.49 in, 1.231646 m
TCG	0.00 in
VCG, below deck	0.09 in, 0.0023 m (0.25 in from report)
GML	18.6 in
Moment of Inertia in Pitch	20.566 slugs-ft2
Moment of Inertia in Roll	2.782 slugs-ft2
Radius of gyration in Pitch	28.44% 2.36 ft
Radius of gyration in Roll	42.25% 0.87 ft
Roll period, model scale from roll decay test	3.66 sec

3. NUMERICAL SIMULATION

The commercial CFD code STAR-CCM+, developed by CD-adapco, was utilized to create numerical simulations correlating to the model tests. STAR-CCM+ uses a finite volume method (FVM) to represent and evaluate partial differential equations. Components in which STAR-CCM+ contain are automated meshing technology, physics modeling, and integrated post processing.

3.1 GOVERNING EQUATIONS

The simulations of the computational model were solved as isothermal and neglecting viscosity. Viscous effects would have added to computation time by increasing the number of volumetric cells in the simulation and were not of importance when characterizing the differences in results with and without the overset meshing technique applied. Therefore, the important flow physics of the computational model could be determined by solving the Euler equations for the fluid flow with the inclusion of body forces related to gravity. The Navier-Stokes equations are given by

$$\frac{\partial u_i}{\partial t} + u_j \frac{\partial u_i}{\partial x_j} = -\frac{1}{\rho} + \frac{\partial p}{\partial x_i} + \nu \frac{\partial^2 u_i}{\partial x_j x_j} + \frac{1}{\rho} F_i \tag{5}$$

where u is the velocity, ρ is the density, p is the pressure, ν is the kinematic viscosity, and F is an external body force taken from Newman [5].

By neglecting,

$$\nu \frac{\partial^2 u_i}{\partial x_j x_j}, \tag{6}$$

the viscous terms or shear in Equation 5, the Euler Equation is formed.

$$\frac{\partial u_i}{\partial t} + u_j \frac{\partial u_i}{\partial x_j} = -\frac{1}{\rho} + \frac{\partial p}{\partial x_i} + \frac{1}{\rho} F_i \tag{7}$$

Therefore, only the continuity equation and momentum equations, in each of the three dimensions, will be solved. By solving these equations, the local pressure and velocity components can be obtained. The Eulerian Multiphase model within STAR-CCM+ is used to separate and solve the governing equations between water and air. The water is modeled as an incompressible fluid while the air is modeled as a compressible ideal gas.

3.2 VOLUME OF FLUID MODEL

In order to capture the interactions between the air and water of the free surface, the Volume of Fluid (VOF) method model is utilized within STAR-CCM+. The VOF method is suited to simulating flows of several immiscible fluids on numerical grids capable of resolving the interface between the phases of mixture (such as free surface flows). The spatial distribution of each phase is given by a variable called the volume fraction, which sums to one for each cell. In this case, the free surface is defined as the level where the volume fractions of air and water are both equal to 0.5. It is desired that the free surface remains a sharp interface. In order to resolve the sharp interface of the free surface, a discretization scheme is needed to approximate large spatial variations of phase volume fractions. The High-Resolution Interface Capturing (HRIC) scheme tracks a sharp interface due to its design to mimic the convective transport of the immiscible fluid components. A more in-depth analysis of the VOF method and HRIC can be found in Hirt and Nichols [6].

VOF waves are used with the VOF multiphase model within STAR-CCM+ and simulate surface gravity waves on the air and water interface. The water and air divisions within the computational domain were initialized by selecting an appropriate free surface level. This free surface level was chosen near the natural waterline of the SES, when on cushion. Instead of giving the SES a longitudinal component of velocity, the current and wind, of the water and air respectively, are given initial velocity values. STAR-CCM+ allows five different options for surface gravity waves to be utilized during simulations (flat, first order, fifth, order, superposition, or irregular). Flat waves, which correspond to calm water, were chosen for all simulations in this thesis due to the rigid skirt configuration of the SES. All other wave cases produce plowing of the SES since the rigid seals do not contour to the water surface, which can be seen in Donnelly [1]. The full model SES geometry can be seen in Figure 3. The yellow areas in the top image of Figure 3 denote the locations of the momentum sources.

3.3 6-DOF SOLVER

STAR-CCM+ contains a six degree of freedom solver (6-DOF) that can be enabled for calculating the rigid body response to the time varying forces and moments imposed on the body by the computed flow. The model requires mass, moment of inertia, and initial conditions to be specified. The 6-DOF solver allows the body to move freely in all degrees of translation and rotation. The meshing technique selected will signify the movement of the computational domain. With the traditional meshing technique, the entire computational domain moves with the body centered local coordinate system while the incoming flow remains moving relative to the global coordinate system. The overset meshing technique only requires the overset region to move with the body centered coordinate system, while the larger computational domain and the incoming flow move relative to the global coordinate system. Both techniques will preserve the mesh. However, only two degrees of freedom were allowed for the computational model. The model was allowed to translate in the vertical direction in heave and to rotate around the y-axis in pitch.

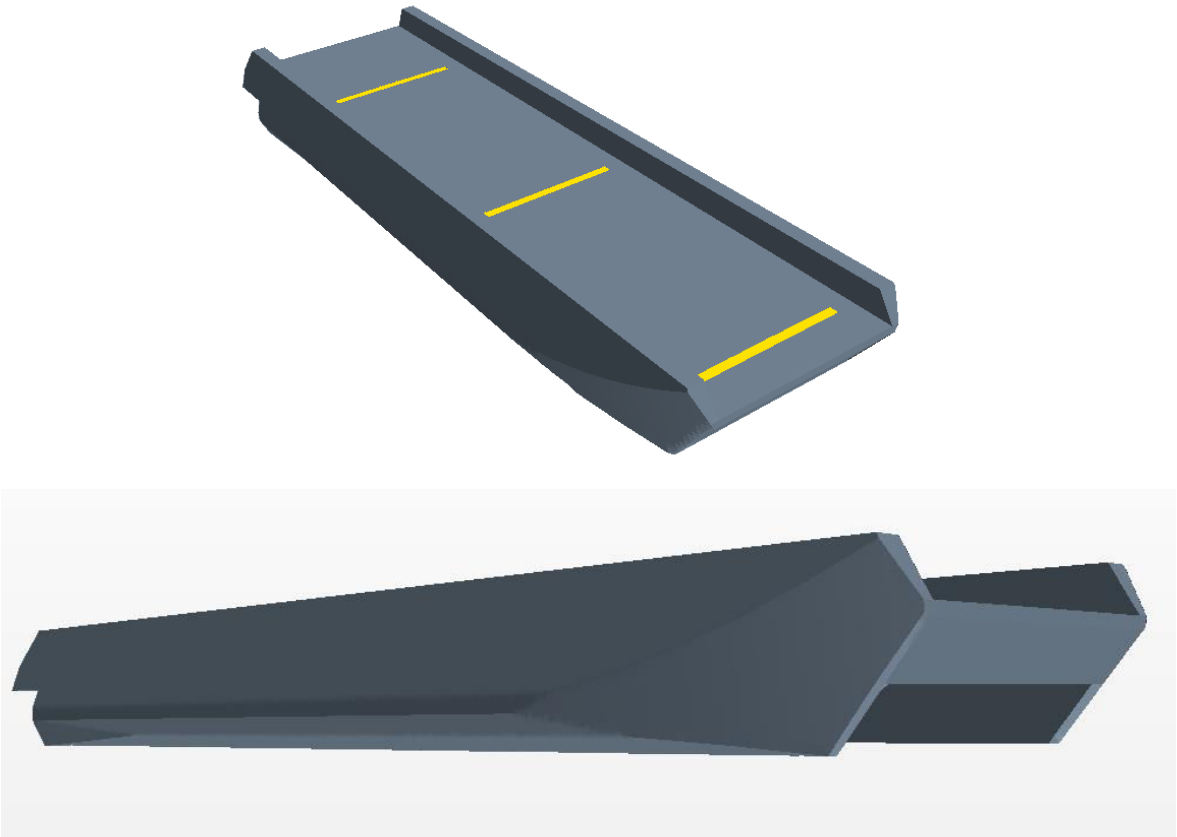

Figure 3: Full T-Craft geometry as modeled in the simulations.

3.4 USER-DEFINED FIELD FUNCTIONS

STAR-CCM+ allows the capability of implementing user code in various ways. User-defined field functions were the only method of code manipulation used in this work. User-defined field functions access field data or create more complex initial conditions. The cushion pressure of the SES was initialized using a user-defined field function. Since computation time of these simulations are expensive, the initialization of the free surface close to the waterline of the SES in conjunction with the initialization of cushion pressure produce solutions that approach a steady state at a faster pace. Other user-defined codes were developed for monitoring drag components on the SES and post processing for free surface elevation contours.

3.5 COMPUTATIONAL DOMAINS

Two separate computational domains needed to be constructed in order to evaluate the solution with a traditional meshing technique and an overset meshing technique. For the computational model with the traditional meshing technique, the computational domain consisted of a half-model bounded by a rectangular prism with a symmetry plane cutting through the centerline of the T-Craft geometry. The domain extends a little more than one ship length in front, behind, below and in the transverse direction of the T-Craft. The top face of the domain is slightly less than a ship length above the T-Craft. The computational domain is much smaller than generally required when working with a free surface, three to four ship lengths behind the craft and two to three in front of the craft. This was done to reduce the cell count of the simulation and save computation time. Although accuracy in the far field may be corrupted, this smaller domain was deemed suitable since the free surface effects around the hull and under the cushion were the main focus of this initial comparison between the overset and the traditional meshes. The forward, bottom, and side faces of the rectangular prism are velocity inlets. The aft face is a pressure outlet for the allowance of the fully developed flow field through the domain without the reflection of wake energy. The top face is also a pressure outlet in case air from the top is needed by the momentum sources. The computational domain (bow facing right), with the traditional mesh, can be seen in Figure 4, taken from Donnelly [1]. In the computational domain, the red represents the velocity inlets, blue represents the symmetry plane, and orange represents a pressure outlet.

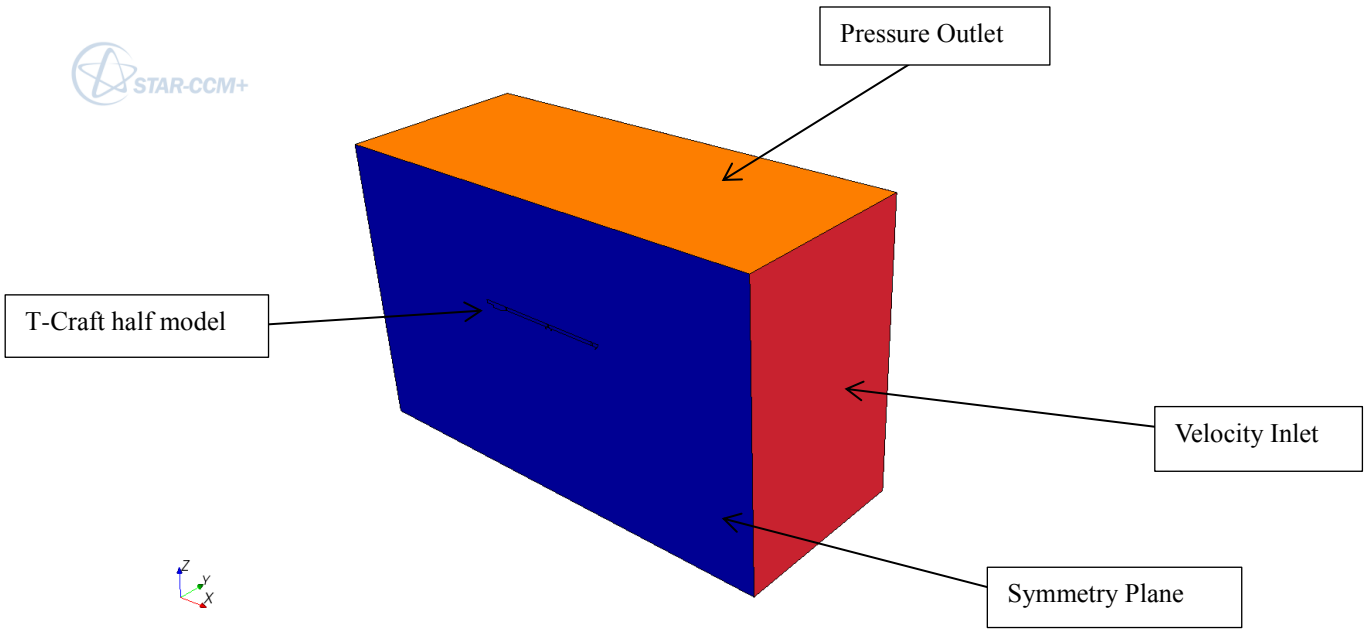

Figure 4: Computational domain without overset meshing technique.

The computational domain for the overset meshing technique varies slightly from the previously discussed one. Instead of consisting of just one rectangular prism, the overset computational domain contains two rectangular prisms with a smaller rectangular prism entrenched in the larger one. The larger rectangular prism is known as the background region and the smaller one as the overset region (Figure 5). It is of particular importance to note the extension of the overset region forward, aft, and transverse to the SES. In order to ensure higher accuracy of the solution, the boundaries of the overset region should be placed in areas with smoother solutions.

The background region consists solely of the boundary conditions (the velocity inlets and pressure outlets), whereas, the overset region consists solely of the T-Craft half-model. Although the overset region is fully entrenched within the background region, they are to be considered two separate entities. Therefore, the background region and overset region need to be coupled and is thus achieved through a linear interpolating interface in the acceptor cell region to be discussed below.

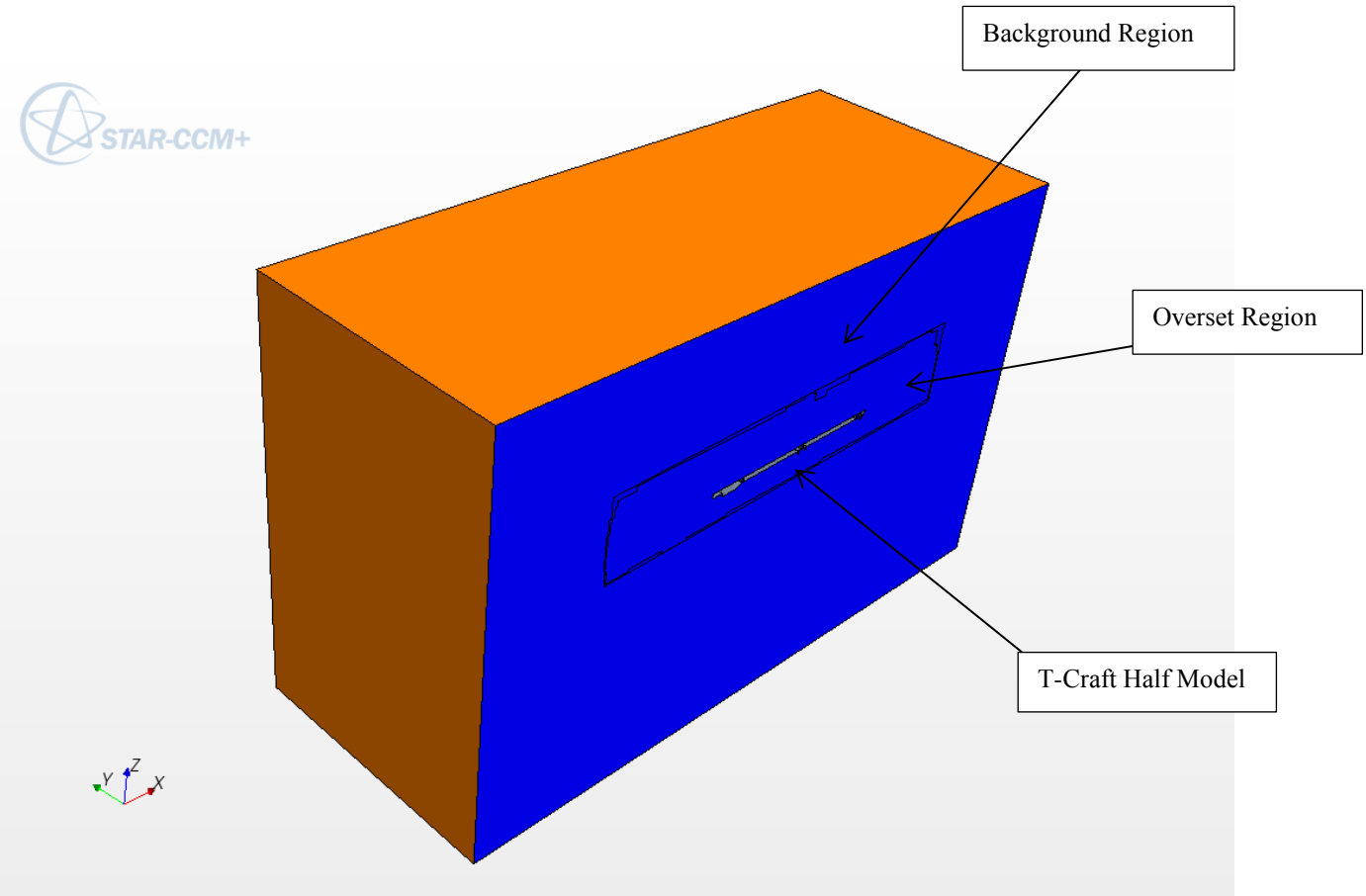

Figure 5: Computational domain for overset meshing technique.

3.6 TRANSIENT AND CONVECTIVE SCHEMES

The simulations consisted of an implicit unsteady solver with a first-order temporal discretization scheme. The implicit unsteady solver is required since the volume of fluid method is time dependent and is solved using a segregated flow model. The basis of the VOF method is understood by considering the amount fluid volume fluxed through a cell during a time-step (Hirt and Nichols [6]). Each time-step contains inner iterations which converge the solution at that instant in time. The simulation then updates at each time-step as it marches through time. The time-step and inner iteration numbers varied from simulation to simulation based on the initial conditions of the flat wave. The smaller the time-step the fewer number of inner iterations are needed to converge the solution. The time accuracy of the solution is driven by the Courant-Friedrichs-Lewy (CFL) number.

$$CFL = \frac{U\delta t}{\delta x} \tag{8}$$

The CFL number relates the characteristic velocity (U) and the time-step (δt) to the grid size (δx). CFL values less than or equal to one yield a solution that limits the fluid from moving through more than one grid space or cell size per time-step. However, CFL numbers greater

than one still may produce a viable solution as long as it is not time dependent. A second-order upwind scheme is used for the convection term. Velocity values are linearly interpolated from cell values on either side of the face with reconstruction gradients.

3.7 MODELING SKIRTS AND FANS

The SES model within the numerical simulations is a simplified hullform. Due to the complexity of modeling dynamic and flexible skirts within STAR-CCM+, a simplified rigid skirt approximation is made. The skirts are modeled as rigid flat plates and are shortened to the waterline of the craft. This enables the SES the ability to maintain cushion pressure with minimal interaction of the skirts and the free surface. However, there is a gap between the free surface and the rigid seal which results in air leakage from the cushion out the bow of the SES. The problems that arise with the skirts having an improper seal with the free surface are discussed later in the report. Dynamic modeling of flexible skirts with a free surface is a complex problem, therefore, not within the scope of this work. Practicality of the overset meshing technique, itself, is the main focus of this work and may give insight to tackling the challenging problem of dynamic modeling of flexible skirts.

Momentum sources were used to model the fans of the SES and maintain a constant cushion pressure, which reflected the cushion pressure seen in the experimental results. Momentum sources are volumes which have a constant value of momentum passed through them in a desired direction. When changes in pressure due to air cushion leakage occur, the momentum source adjusts the volume flow accordingly. The change in momentum through the momentum source is equal to the force on the bottom face divided by the volume of the momentum source. The accuracy of the momentum source simplification can be seen in Donnelly [1].

There was an undesirable pressure leakage from the front cushion due to the rigid skirt configuration. Excess pressure leaks out of the front of craft which periodically pitches the craft downward. Then the pressure begins to build back up creating a jet of higher velocity air to blow through the now smaller clearance which causes the SES to pitch back upward. This cycle continues and is the major source of the unsteadiness in these simulations. This leakage out of the front of the craft causes the front momentum source to pump in air at a high rate to maintain cushion pressure.

To reduce the strength of the “jet,” the front momentum source was relocated from right behind the front skirt to the middle of the front cushion. Also, the width of the momentum source was increased by four times its original value to decrease the velocity of the flow out of the momentum source (Figure 6). Modifying the momentum source location and size steadied the cushion pressure, which in turn, steadied the pitch movements of the SES.

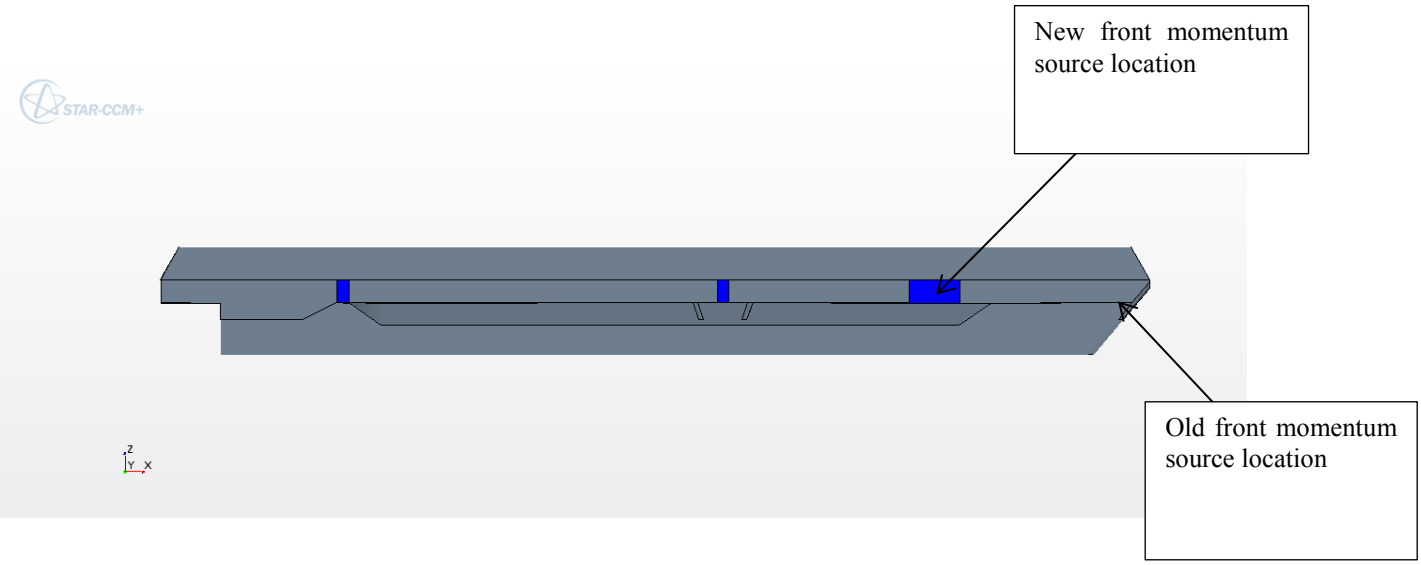

Figure 6: Profile view of SES showing new front momentum source with comparison in size to middle and rear momentum sources.

4. OVERSET MESHING TECHNIQUE

Studies that involve the overset meshing technique have a background region enclosing the entire solution domain and one or more smaller regions containing the bodies within the domain as seen in Figure 7.

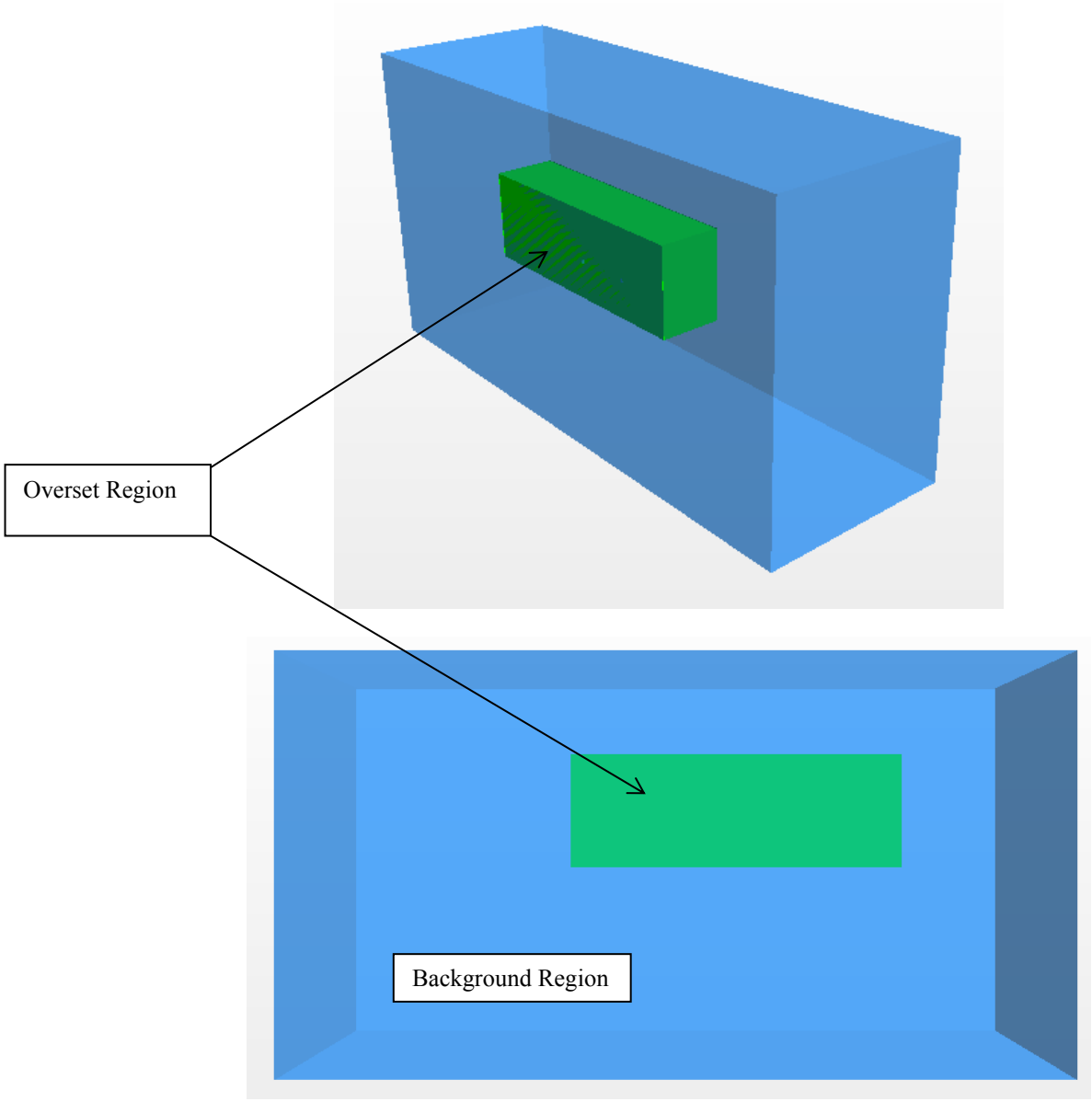

Figure 7: Schematic of overset and background regions.

Within a domain containing an overset mesh, cells have three groupings: active, inactive, or acceptor as seen in Figure 8. The red color represents inactive cells, the yellow color represents active cells, and the blue color represents acceptor cells.

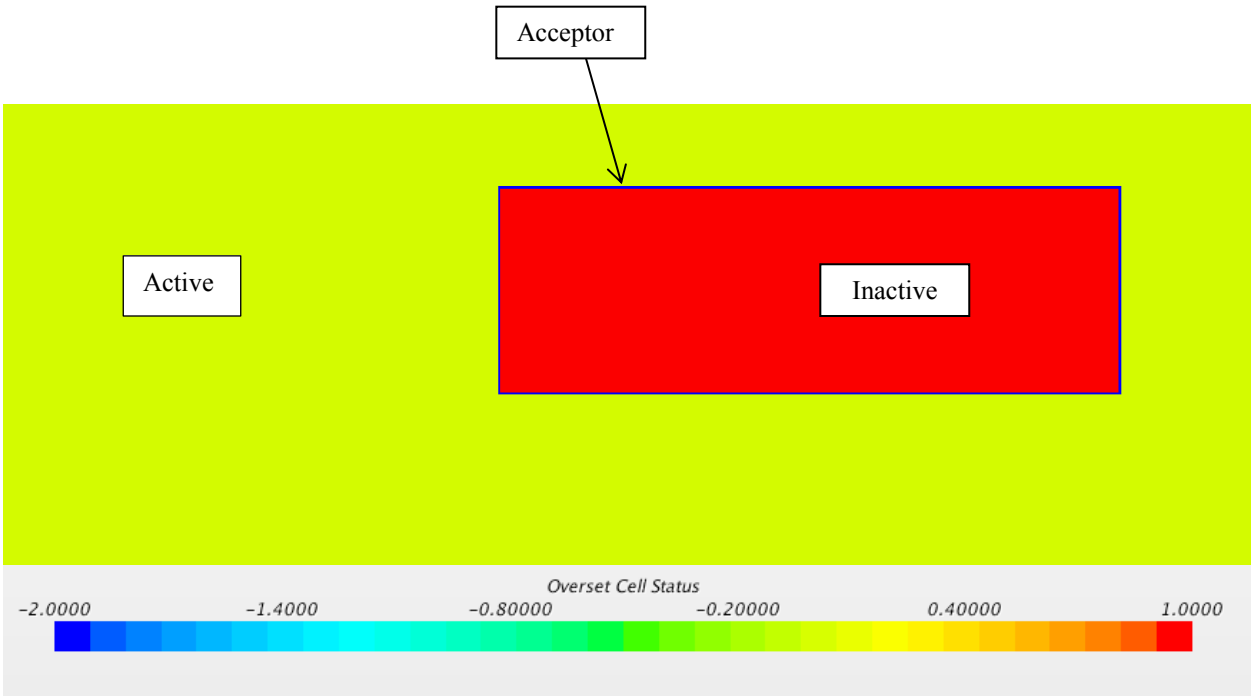

Figure 8: Representation of active (yellow), inactive (red), and acceptor cells (blue) in the background grid.

The discretized governing equations are solved in the active cells. No equations are solved within the inactive cells but there is potential for the inactive cells become active cells if the overset region is moving relative to the background region. The active and inactive cells are separated by the acceptor cells in the background region which are attached to the overset boundary in the overset region. These acceptor cells are used to couple solutions on overlapping grids. Acceptor cells of one mesh interpolate dependent variable values from four donor cells, or active cells, of the other mesh in the overlapping region. Weighted linear interpolation was done between the overset and background regions using shape functions spanning a tetrahedron defined by centroids of the donor cells. The interpolation function are built into the coefficient matrix of the linear equation system and can be solve simultaneously with the discretized equations from the STAR-CCM+8.02.011 help guide [7]. This approach ensures an implicit and a strong coupling of the overset and background meshes. The variable value in the acceptor cell is described as:

$$\Phi_{acceptor} = \sum \alpha_i \phi_i \tag{9}$$

where α_i is the weighting factor and ϕ_i is the variable values of the donor cell for i running over all donor nodes of the interpolation element. It is also of importance to note that the cells of the overlapping grids should be similar in size. The accuracy of the solution can be degraded if cell sizes are significantly different due to the inability of a coarser grid to resolve the same flow features of a finer grid. The discretization error during interpolation will be on the error level of the coarser mesh. A more thorough explanation of the overset mesh methodology within STAR-CCM+ is provided in Hadzic [8].

The overset mesh is practical for parametric design studies, objects with extreme ranges of motion, and interaction between two or more objects. In a simulation without the overset meshing technique, the entire domain moves with a body fixed coordinate system while the flow remains relative to a global coordinate system.

Although the overset mesh has its practical uses, it requires a simulation run time much greater than a non-overset mesh. An overset meshing technique will generally require parallel computing for simulations due to its complexity. However, communication between the cells through the interface of the overset region and the background region can only be done in serial within the version of STAR-CCM+ used for this study. This serial computing restraint hinders the attractiveness of the overset meshing technique unless it is absolutely necessary for computational studies.

4.1 IMPLEMENTATION OF OVERSET MESH ON SES

A baseline simulation similar to that of Donnelly [1] was produced with a traditional meshing technique featuring a hexadral mesh applied to the fluid domain and the SES geometry. A new simulation was then produced including the overset region with all other specifications unaltered (i.e. physics and meshing criteria). Figure 9 and Figure 10 depict the overset cell status in the overset and background regions respectively. As previously stated, the active cells are indicated by yellow, inactive by red, and acceptor by blue. Arriving upon an accurate solution within the computational domain requires an adequately refined mesh. In order to accurately determine a correct grid resolution, a grid convergence study was performed on a series of systematically refined meshes for both the traditional meshing technique and the overset meshing technique. The grid convergence study for the traditional meshing technique can be seen in Clark [9]. Grid convergence for the overset meshing technique was done using the steady state resistance solutions on the three grids seen in Table 2. Medium and coarse meshes were produced by increasing the cell size of the fine mesh with a refinement factor, $\boldsymbol{r_k = \frac{\Delta x_{g2}}{\Delta x_{g1}} = \frac{\Delta x_{g3}}{\Delta x_{g2}} = \sqrt{2}}$, where $\boldsymbol{\Delta x_{g3}}$ is the grid spacing of the coarse grid, $\boldsymbol{\Delta x_{g2}}$ is the grid spacing of the medium grid, and $\boldsymbol{\Delta x_{g1}}$ is the grid spacing of the fine grid.

Solution verification was done using a Richard Extrapolation, as seen in Xing and Stern [10], to determine the error estimates associated grid spacing. Steady-state resistance on the body was the metric of interest when determining solution verification. Solution changes ε between the grid levels can be seen by Equations 10 and 11.

$$\boldsymbol{\varepsilon_{k_{21}} = S_{k_2} - S_{k_1}} \tag{10}$$

$$\boldsymbol{\varepsilon_{k_{33}} = S_{k_3} - S_{k_2}} \tag{11}$$

$$\boldsymbol{R = \frac{\varepsilon_{k_{21}}}{\varepsilon_{k_{33}}}} \tag{12}$$

where S_k is the solution for the k study (g for grid in this case) and 1, 2, and 3 are the refinement levels for the fine, medium, and coarse grids respectively. The convergence ratio R, seen in Equation 12, determines the convergence condition. Monotonic convergence $0 < R < 1$ enables the use of the Richardson extrapolation to determine the observed order of accuracy p_k, error estimate $\delta^*_{RE_{k_1}}$, and the numerical benchmark S_c.

$$\boldsymbol{p_k} = \frac{\ln(\frac{\varepsilon_{k_{33}}}{\varepsilon_{k_{21}}})}{\ln(r_k)} \tag{13}$$

$$\boldsymbol{\delta^*_{RE_{k_1}}} = \frac{\varepsilon_{k_{21}}}{r_k^{p_k}-1} \tag{14}$$

$$\boldsymbol{S_c} = \boldsymbol{S_{k_1}} - \boldsymbol{\delta^*_{RE_{k_1}}} \tag{15}$$

When p_k equals the theoretical order of accuracy p_{th} the solutions are in the asymptotic range. The observed order of accuracy was found to be 1.14, which is not close to the theoretical order of accuracy of 2. The Richardson extrapolation error estimate is roughly 0.78 lbf for the full model. This yields a generalized relative error, $\delta^*_{RE_{k_1}}/S_{k_1}$ of 13 percent. For cases where the observed order of accuracy and theoretical order of accuracy are far apart (such as the case of the overset meshing technique), a correction factor can be applied. The correction factor is used as a metric for defining the distance from the asymptotic range.

$$\boldsymbol{CF} = \frac{r_k^{p_k}-1}{r_k^{p_{th}}-1} \tag{16}$$

The new error estimate $CF\delta^*_{RE_{k_1}}$ becomes 0.38 lbf and the generalized error estimate is calculated as approximately 6 percent. Problems arise when using this correction factor as a metric for defining the distance from the asymptotic range because it is a function of the refinement factor, r_k. This means for the same observed and theoretical order of accuracies a different correction factor could be used. To avoid this problem, a different metric based on the ratio between the observed order of accuracy and theoretical order of accuracy P can be used for defining the distance from the asymptotic range.

$$\boldsymbol{P} = \frac{p_k}{p_{th}} \tag{17}$$

Now the new error estimate $P\delta^*_{RE_{k_1}}$ becomes 0.45 lbf and the generalized error estimate is calculated as approximately 8 percent. The overset meshing technique yields an error two times more than the traditional meshing technique. The difference in error can most likely be

attributed to the non-conservative interface between the overset and background regions and the smearing of the waterline shown later in this work.

Table 2: Mesh Refinement Specifics.

(m)	Fine	Medium	Coarse
Base Size	2	2.828427	4
Volumetric Control	0.02	0.028284	0.04
Hull Surface Size	0.01	0.014142	0.02
Number of Cells	2570982	1047877	425658

The base size is the largest allowable cell size in the domain and is set as two meters for both simulations. A volumetric control is used to specify the cell size of the waterline for refinement and, consisted of a cell size of two centimeters as seen in Clark [9]. However, a reduction of surface cell size from one centimeter to half a centimeter on the SES hullform was deemed necessary. This reduction in surface cell size provided more reliable resistance and pitch solutions without adding an excessive number of additional cells to the overall simulation.

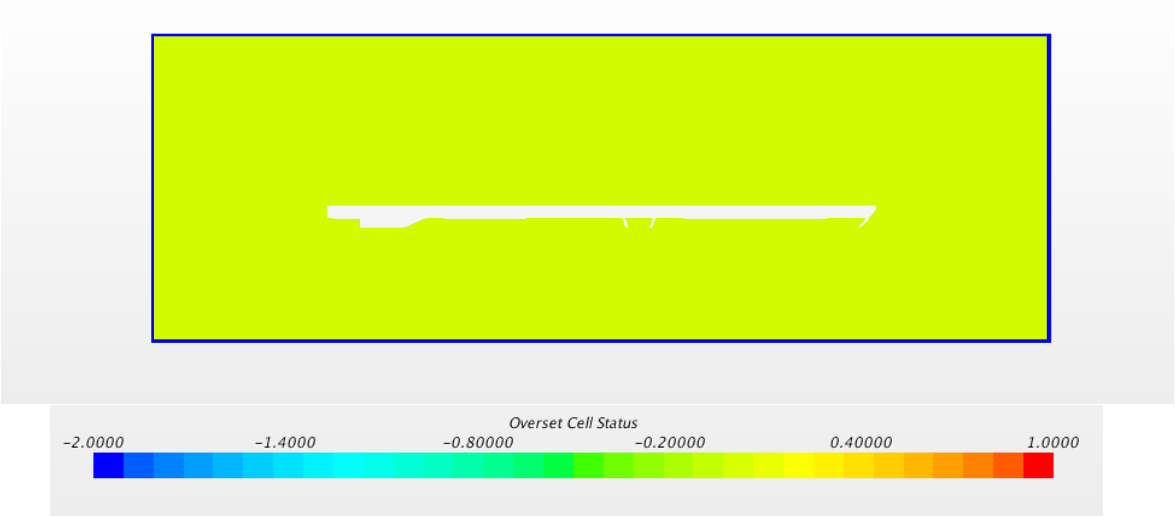

Figure 9: Overset Region Cell Status—active cells in yellow and acceptor in blue.

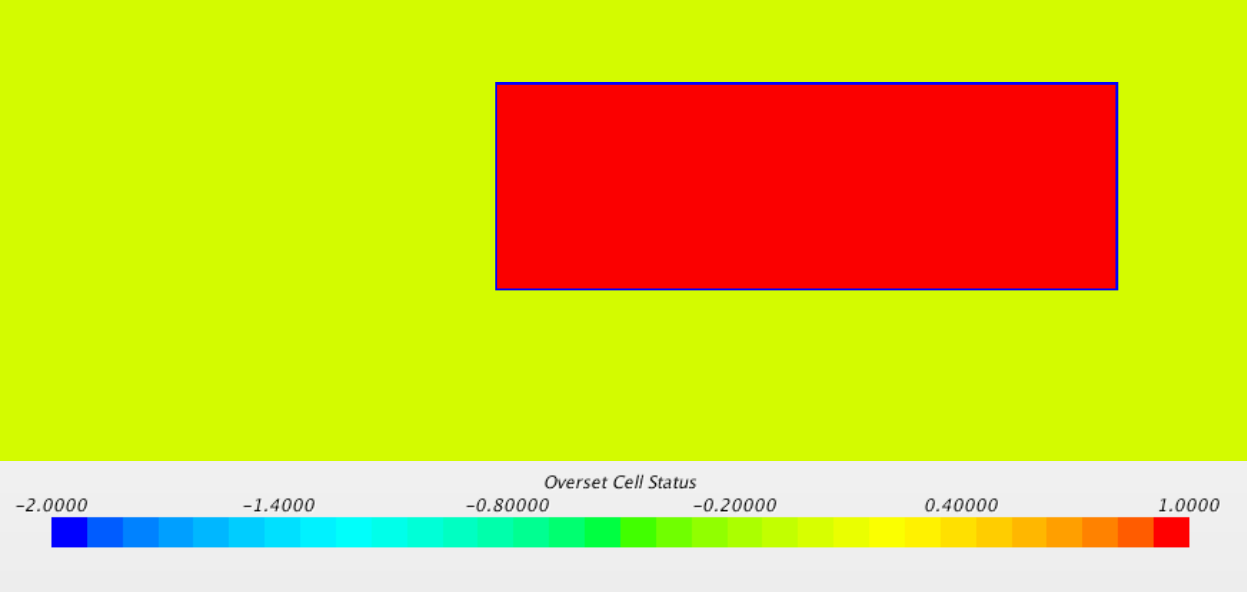

Figure 10: Background Region Cell Status—active cells in yellow, inactive in red, and acceptor in blue.

4.2 PARALLEL COMPUTING

Since both simulations contain millions of cells, a supercomputer was employed to reduce CPU time through parallel computing. This was made possible through Advanced Research Computing at Virginia Tech. The supercomputer consists of a 318-node Cray CS-300 cluster. Each node is outfitted with two octa-core Intel Sandy Bridge CPUs and 64 gigabytes of memory. Both simulations utilized eight nodes with sixteen processors per node and comparisons of CPU time were made. The overset simulation had a CPU time 3.67 times longer than that of the non-overset mesh. One second of simulation time using the overset mesh required 275 minutes of CPU time, whereas, one second of simulation time using the non-overset mesh required only 75 minutes of CPU time. However, the newest version of STAR-CCM+, Version 9.04, does yield a speed up of the overset meshing process. With the newest version of STAR-CCM+, one second of simulation time now requires 206 minutes of CPU time. This is a 25 percent speed up from its predecessor.

4.3 COMPARISON OF OVERSET MESHING TECHNIQUE

The newly generated overset region (red mesh) overlapping the background region (blue mesh) can be seen in Figure 11 and Figure 12. The comparison of the overset meshing technique with the traditional meshing technique was performed using a simple test case of the craft advancing in calm water. The incoming flow was given an initial velocity to correlate to a Froude number of 0.6 and the craft was allowed to move in heave and pitch. Two metrics, drag and pitch, were compared between the baseline simulation and the overset mesh simulation. Results were averaged from four to nine seconds. This was the point where the flow was fully developed and the simulation had reached a quasi steady state with little variation in the drag.

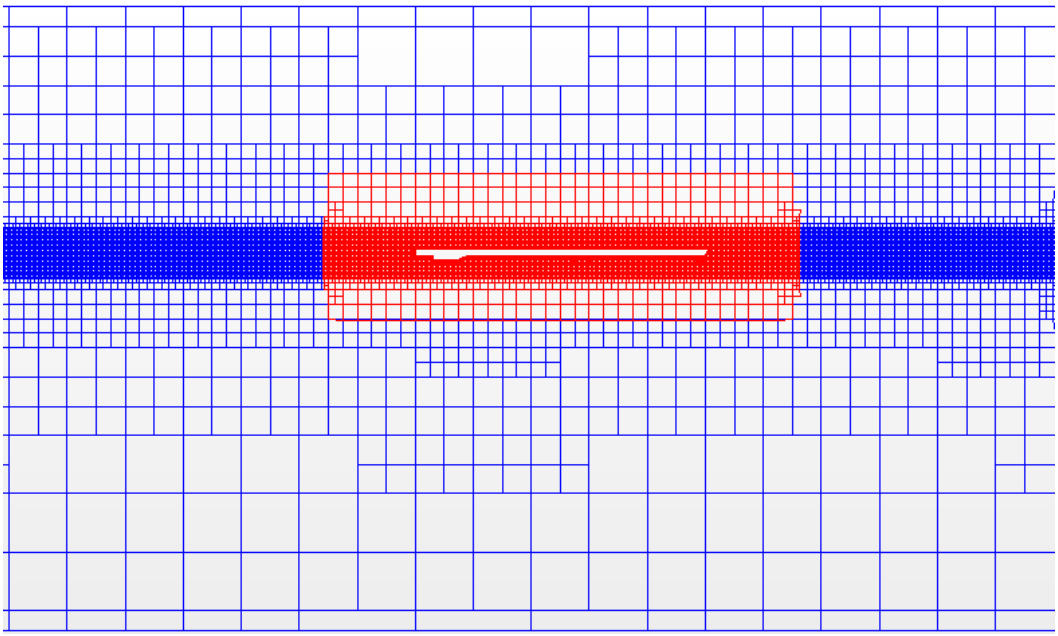

Figure 11: Mesh differentiating between the overset (red) and background (blue) meshes.

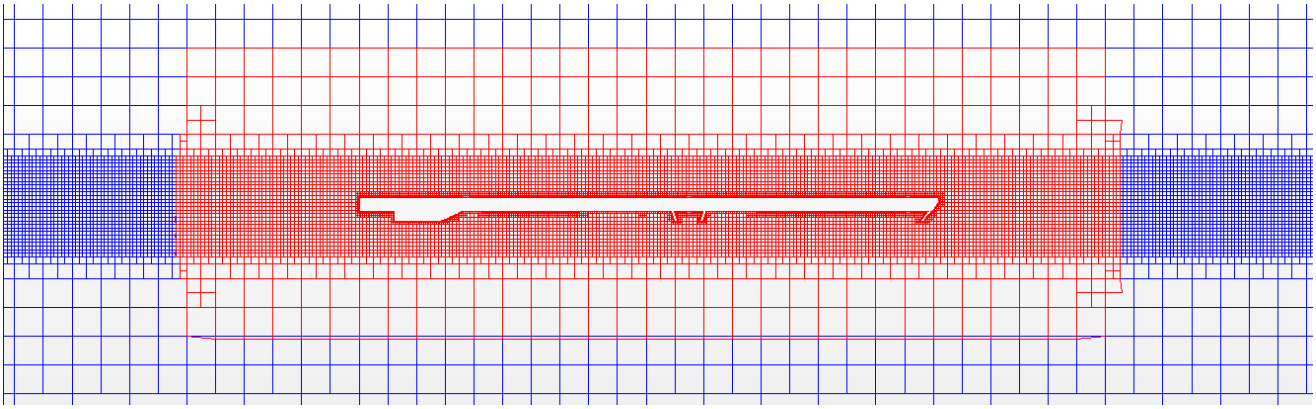

Figure 12: Magnified view of the overset (red) and background (blue) meshes.

The major discrepancy between the two wake profiles is the free surface elevation in front of the overset region. This can be seen by comparing the free surface elevation contours forward of the SES in Figure 13 and Figure 14. That contour in Figure 14 marks the beginning of the overset region. Variations in free surface elevation between the two simulations influence the pitching nature of the craft.

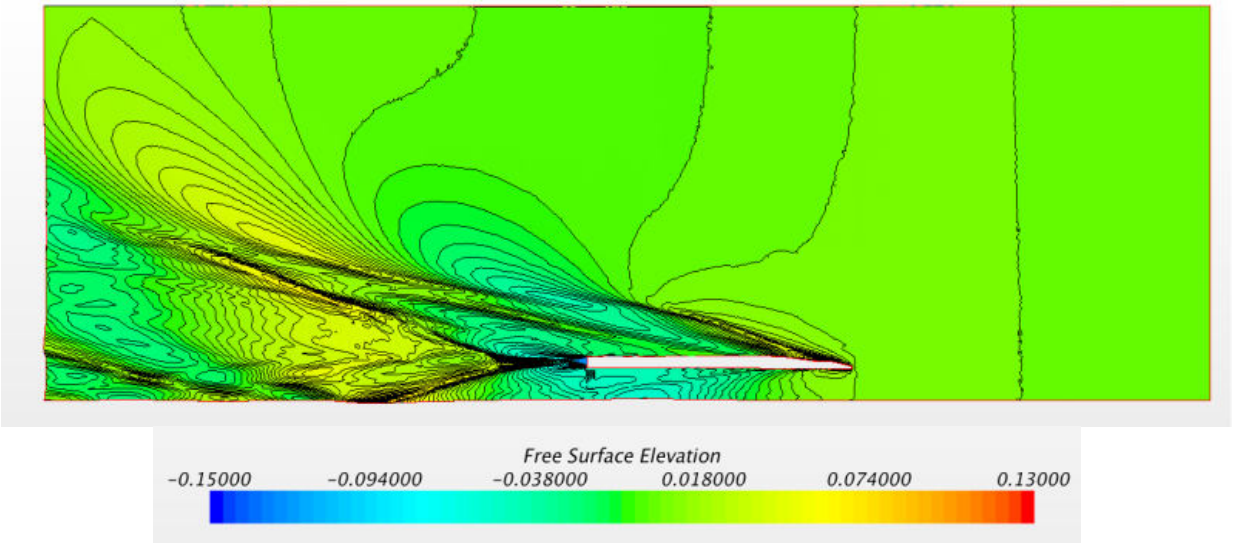

Figure 13: Free surface elevation contours scene of non-overset, single mesh simulation—half model.

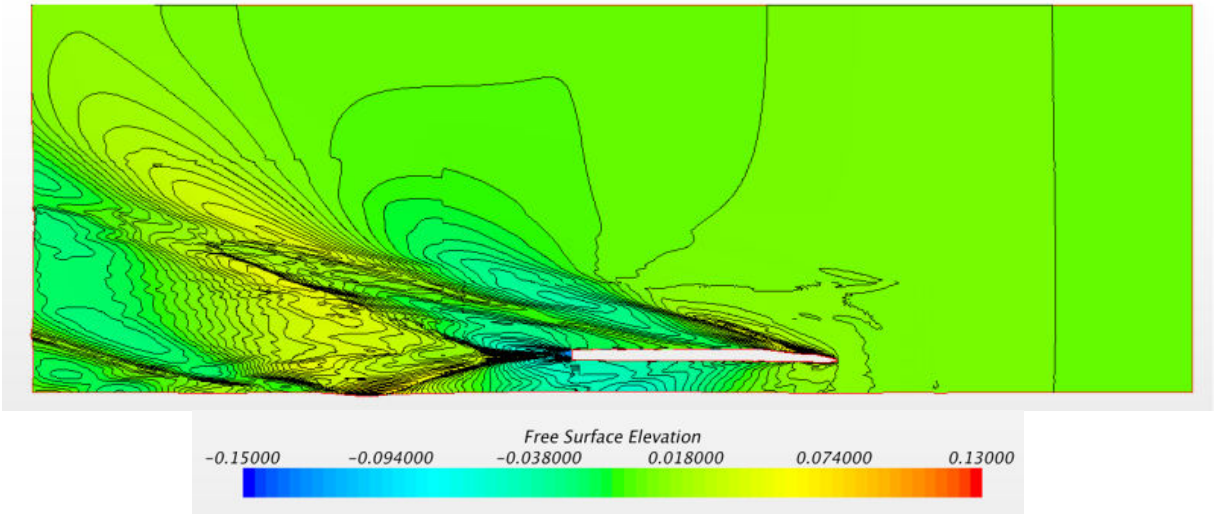

Figure 14: Free surface elevation contours scene of simulation with overset mesh—half model.

Figure 15 shows the small differences in pitch between the baseline simulation and the overset mesh simulation. The overset mesh slightly increases the average pitch magnitude.

Negative pitch represents a bow up condition. The average pitch in the baseline (no overset) simulation is -1.72 degrees; whereas, the average pitch in the overset simulation is -1.88 degrees. This represents a difference in height of the bow of 0.36 cm which is small compared to the cell size of 2.0 cm in that region.

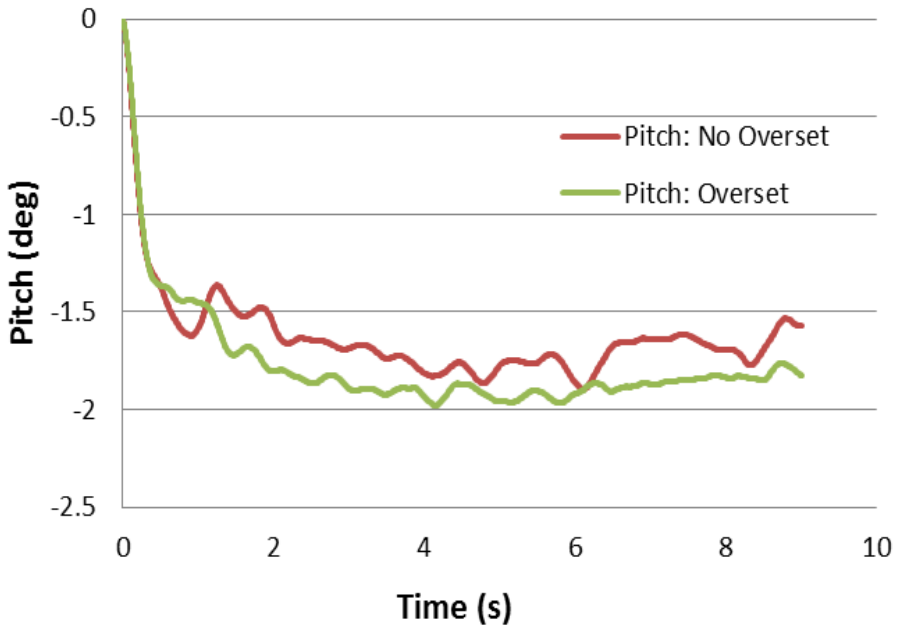

Figure 15: Plot of pitch differentiating results between overset and non-overset meshes.

The pitch seems to be offset by a fraction of a degree (with a few outliers) between the baseline and overset simulations. This is apparently due to the interpolation that occurs between the overset and background regions within the overset simulation. The interpolation between the overset and background regions causes a disturbance that propagates both upstream as well as downstream, leading to a smearing of volume fraction at the waterline directly ahead of the overset region (Figure 16).

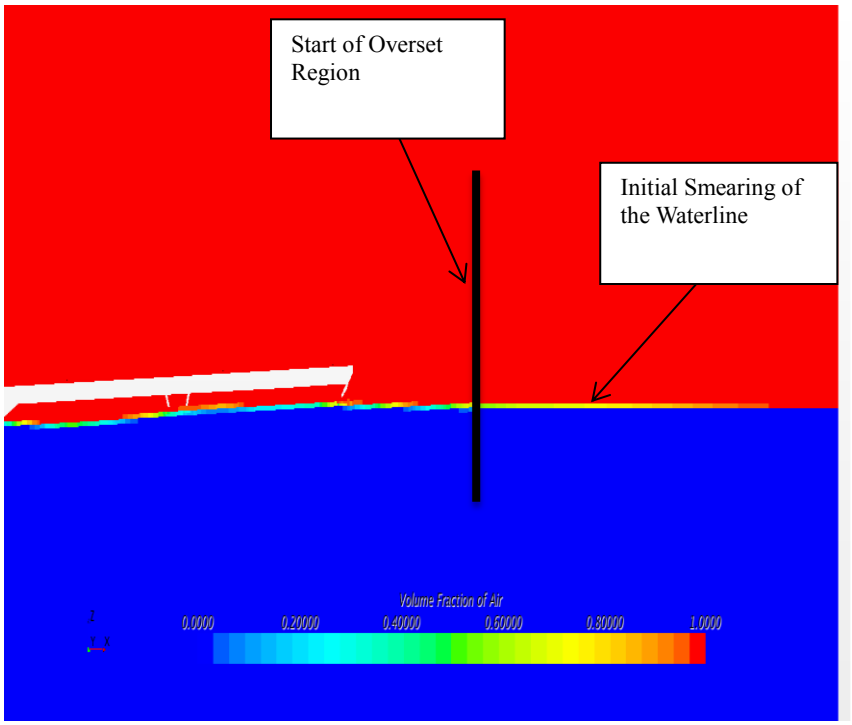

Figure 16: Volume fraction scene showing smearing of incoming free surface.

This is due to the discontinuous nature of the free surface during interpolation between the overset and background regions. Since interpolation of volume fraction must occur within the acceptor cell region, it is likely donor cells of each mesh will span both sides of the free surface yielding a smearing of the waterline.

This smearing creates undesirable volumetric cells along the waterline. A few cells being modeled incorrectly forward or aft of the craft could lead to the observed variation in results; especially, when the movement of the craft is on the same magnitude as the mesh size. Further refinement of the waterline in front of the craft may be needed in future cases to reduce this effect. Smearing along the waterline should not detract from the usefulness of the overset meshing technique. The ability of the region to move relative to nearby or encompassing regions is of primary importance. The refinement of the mesh on the hull surface resolves the flow characteristics around the body and mitigates the adverse effect of the waterline smearing.

The increase in pitch should yield an increased drag value for the overset simulation since a larger aft component of the pressure acts on the underside of the hull as the pitch is increased. However, this is not the case when examining Figure 17. The average drag values between the baseline and overset simulations converge within 0.85 percent of each other. After multiple seconds of simulation time, the smearing or free surface build-up spreads ahead of the overset region. The smearing generates a slightly higher incoming free surface elevation which the craft will reorient itself upon (Figure 16). Since STAR-CCM+ measures the angle of the body from its initial orientation, a slightly higher pitch angle is measured by the overset simulation to maintain the same cushion pressure and aft component of drag force as seen in the baseline simulation (approximately a gauge pressure of 200 Pascals). As seen in previous work done by Donnelly and Neu [11], the wavemaking drag due to the hull pressure will steadily increase with

Froude Number until a hump speed is reached. Since the Froude number of both simulations is the same, the wavemaking drag produced should remain consistent. Drag was the primary metric for comparison of the overset meshing technique. As previously stated, the overset meshing technique is required for relative motion between two bodies. Even though the overset meshing technique may produce undesirable volumetric cells and an alteration in pitch, it is necessary for SES motion relative to the static domain bottom in shallow water simulations.

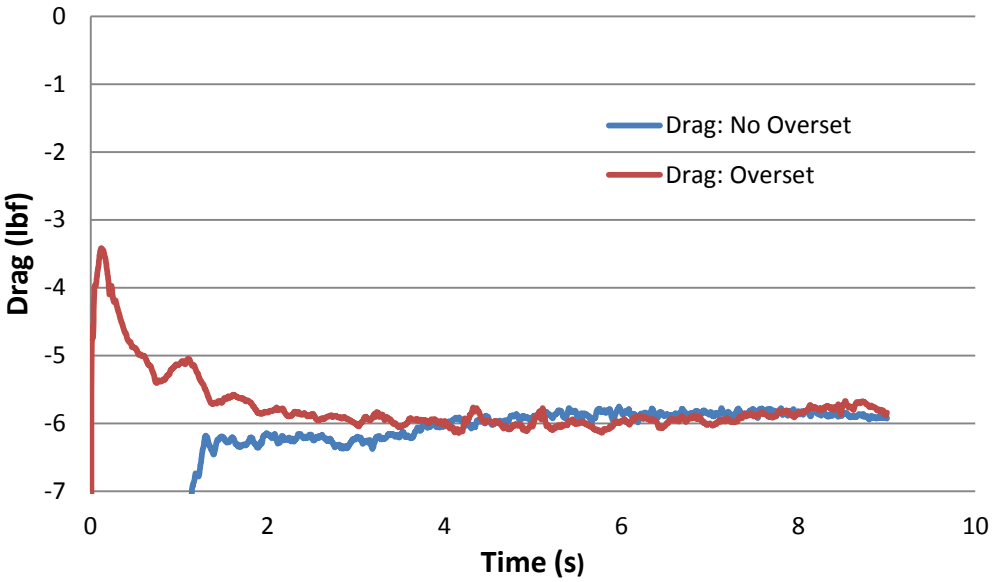

Figure 17: Plot of drag differentiating results between overset and non-overset meshes.

5. SHALLOW WATER SIMULATIONS

5.1 IMPLICATIONS OF WATER DEPTH ON SES

As shown in Kramer [12], testing of the SES-100 and SES-200 craft determined a significant variation in resistance between deep and shallow waters. Testing proved deep water assumptions are suitable for a water depth greater than or equal to the cushion length. Shallow water effects become prevalent and need to be considered when water depth is half of the cushion length as noted in Kramer [12]. Early predictor methods for behavior of SES craft consisted of the wavemaking predictions of Newman and Poole [13]. Doctors [14] extended their work by producing a wavemaking prediction analysis using rectangular pressure patches and smoothing functions, for the fronts and sides, to model the SES. Doctors' predictive routine has been extended to give insight to the effects of water depth on the wavemaking resistance of the SES as seen in Bhushan [15]. However, Doctors' approach has limitations when considering the dynamics of the SES.

The remainder of this thesis focuses on implementing CFD techniques to simulate shallow water effects on the wavemaking resistance of a SES model. The commercial CFD code, STAR-CCM+, allows for the complexities of the SES geometry to be modeled along with

the air cushion. As a result, the free surface can be visualized around and under the complex hull geometry and the air cushion. The results obtained using this method should yield a greater understanding of the fluid response in these complicated regions.

5.2 APPLICATION OF OVERSET MESH TECHNIQUE ON SES IN SHALLOW WATER

Relative motion between two bodies requires an alternative meshing technique to be used over a traditional one. This can be achieved through a sliding mesh, deforming mesh, re-meshing, or overset mesh. The overset meshing technique was chosen due to ease at which arbitrary motion can be handled between the overset and background regions. Sliding grids are limited by the common sliding interfaces. No overlapping can occur. The re-meshing approach is computationally expensive since the grid must be regenerated at each time step. Therefore, the flow variables must be interpolated from the old grid to the new grid. This must happen throughout the entire domain. Interpolation within the overset meshing technique only occurs in a limited number of cells, acceptor cells, rather than the whole domain The grid quality of the overset mesh is not affected by the changing orientation of position of the bodies. No skewed cells are introduced into the simulation as may happen with the use of a deforming mesh. Comparisons and advantages/disadvantages of the separate grids are found in Hadzic [8]. However, the overset mesh can also incorporate a sliding or deforming mesh within its region. This is useful when using a coupled fluid structure interaction simulation.

The overset region was shortened in the shallow water simulations to decrease the amount of sweep that occurred between the overset and background meshes. If the sweep angle of the overset region could be held to a minimum then less smearing of the free surface should occur. Shortening of the overset region also saved computation time by reducing the volume of the hole cutting region in the background mesh.

Two approaches could have been taken when applying the overset meshing technique to these shallow water simulations. The first approach would have been to alter the domain depth with a constant incoming flow velocity. This approach requires various domain sizes based on the depth Froude number. Each simulation has a separate mesh with varying cell counts. However, the overset region and mesh within the overset region would remain unchanged. The second approach would be to alter the velocity of the incoming flow with a constant domain depth. Although this approach uses a constant domain size, therefore, a constant mesh, it would be difficult to differentiate between the effects due to the shallow water and the effects due to the ramp in speed since the length Froude numbers will no longer match between simulations. For this reason, a constant incoming flow velocity with alteration in domain sizes was chosen.

Seven alterations to the domain size were done corresponding to seven different depth Froude numbers. Simulations with depth Froude numbers of 0.65, 0.75, 0.85, 0.9, 0.95, 1.0, and 1.05 were produced. Each simulation had an incoming calm water surface with velocity equal to 2.786 m/s. This velocity corresponds to a length Froude number of 0.6 in deep water. As previously stated, all shallow water simulations are inviscid due to the fact that wave making drag is the primary drag component in the evaluation between ship behavior in deep and shallow water. The domain width used in the comparison of the overset meshing technique was not suitable for these shallow water simulations due to the wider wakes produced by the SES. The wider wake interacted with the velocity inlet boundary condition on the side wall in the span-wise direction. By monitoring and comparing the average drag parameter based on a varying

span-wise domain dimension size, convergence can be determined. Three span-wise domain dimensions of 2.5, 3.5, and 5 ship lengths were used. A depth Froude number of 0.9 was selected for all three simulations with varying span-wise domain dimension. The widest wakes generated by the SES occurred at this depth Froude number. Domain size proved to be of importance between 2.5 and 3.5 ship lengths. There was much less dependence on span-wise domain size between 3.5 and 5 ship lengths when comparing the average drag. By taking the average drag value observed in the simulation with a span-wise domain dimension of 5 ship lengths as the "exact" value, the percent error can be determined. The error in average drag of the 2.5 ship length simulation is roughly 11.6 percent whereas, the error in average drag of the 3.5 ship length simulation is roughly 1.2 percent. For the remainder of the thesis, the shallow water simulations use a span-wise domain size of 3.5 ship lengths. This selection saves computation time while ensuring an accurate solution. The extension also provided an improved steadiness to the simulations of all depth Froude numbers. Although, some unsteadiness still persisted for simulations in the critical to supercritical range (Fn_d=0.9-1.05). These critical and supercritical depth Froude number simulations produced a wake which extended to the side boundary. As previously mentioned, the side boundary condition was a velocity inlet with a velocity prescribed in the direction parallel to the SES. The interaction between the orthogonal flows caused reflections of the waves back to the SES producing an enhanced pitch. This called for a different boundary condition to be used on the side boundary.

A pressure outlet was considered for the domain side boundary condition but the perpendicular wake caused reversed flow to occur on several cell faces, meaning the pressure outlet acted as a pressure inlet at these points. At the points of reversed flow on a boundary, the value specified for static pressure will be substituted for the total pressure. This will lead to damping of the waves in the far field and an invalid representation of the free surface throughout the domain. The velocity inlet at the side boundary was also replaced by a symmetry plane. Symmetry planes allow for a zero normal velocity and for values of properties just adjacent to the solution domain to be taken as values at the nearest centroid inside the domain. The symmetry plane preserves the wake generated by the SES at the domain boundary. The larger span-wise computational domain vastly increased the cell count and computation time of the simulations. For this reason, a larger time step of 0.01 with 20 inner iterations was utilized to speed up CPU time since steady state drag was only of interest. Therefore, the solutions are not time accurate.

The new momentum source configuration was used for the latest simulations to produce steadier state pitch and drag results. Each simulation was run and monitored for at least forty-five seconds of simulation time or enough time to produce a steady state. The wider domain created the need for a longer simulation run time to let the flow field fully develop.

5.3 FREE SURFACE ELEVATION CONTOURS OF VARYING DOMAIN DEPTH SIMULATIONS

Shallow water effects become prevalent when the water depth is less than or equal to half the wavelength generated by the SES. Examining the free surface elevation contours can give insight to the behavior of the SES as the water depth decreases. Interactions between the bow and stern wave systems are observed, through these free surface elevation contours, at each of the depth Froude numbers (Figure 18-Figure 24). Each free surface elevation contour uses the same scale for comparison. In the free surface elevation contour figures, the visibility of the hull is turned

off and the white areas represent the part of the rigid side hull that pierces the free surface. Only half-model free surface elevation scenes are shown.

There are slight variations of the wake profiles between depth Froude numbers of 0.65 to 0.75. Minor discrepancies of free surface elevation in the far field aft of the craft can be seen. The wake produced by the SES begins to expand perpendicular to the SES motion at this point. This marks the transition to shallow water phenomena, where the phase velocity depends only on depth i.e. non-dispersive wave motion given in Faltinsen [16]. For the T-Craft model at a length Froude number of 0.6, half the generated wavelength is approximately 1.75 meters. The domain depth at a depth Froude number of 0.65 is roughly 1.87 meters so deep water approximations are valid. On the other hand, the domain depth at a depth Froude number of 0.75 is approximately 1.4 meters which demonstrates the presence of free surface effects when the water depth becomes less than or equal to the wavelength generated by the SES. This can be seen in free surface elevation contours when comparing Figure 18 and Figure 19. As the depth Froude number increases from 0.75, the free surface elevation scenes begin to change drastically. The interaction between the bow and stern wave systems begin to intensify. According to linear shallow water theory, the critical change should occur at a depth Froude number around unity, but the wake profiles offer conflicting results. It can be seen that most interaction between the bow and stern wave systems occurs around Fn_d=0.9 and 0.95 (Figure 21 and Figure 22). Larger troughs, represented by the lighter blue areas, are seen aft of the SES at these two depth Froude numbers. The SES produces a wake almost perpendicular to itself extending outward in the span-wise direction towards the domain side boundary. This is most likely the point at which the critical change occurs. The critical change likely occurs at a point prior to Fn_d=1.0 because of the small length to beam ratio of the SES (l/b=4) and the specified cushion pressure depression to cushion length ratio. The importance of cushion beam to cushion length ratio and its effects on wavemaking resistance can be seen in Yun [3]. Bhushan [15] illustrated the effect of cushion pressure depression to cushion length ratio on location of the primary wavemaking hump. As the cushion pressure is increased the primary hump shifts closer to Fn_d=1.0. After the critical change occurs, the angle of the wake generated by the craft (measured from the craft centerline) decreases and is no longer moving perpendicular to the motion of the SES. The narrowing of the SES wake can be seen when comparing Figures 22-24. In the supercritical regime, the non-dispersive wave motion from the bow and stern systems become evident. All waves, regardless of wavenumber, propagate at the same speed as the disturbance and, therefore, without change in shape. There is little decay of wake amplitude in the lateral distance. This is the reason for the higher free surface elevation propagating outward from the bow wave system in supercritical depth Froude number simulations (Figures 22-24). Narrowing of the bow and stern wave systems as supercritical depth Froude numbers are reached agrees nicely with shallow water theory.

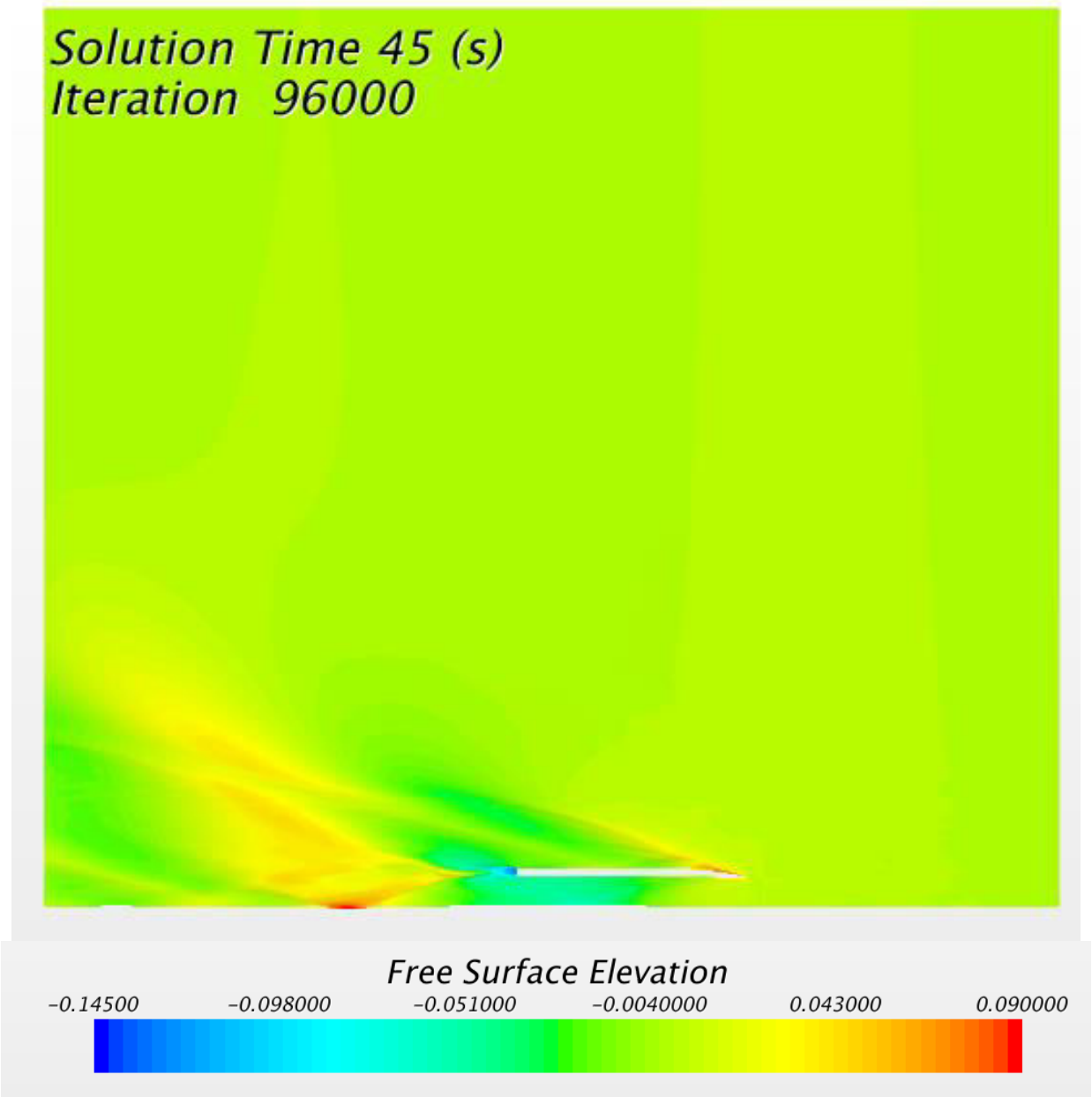

Figure 18: Free surface elevation contours scene of Fn_d=0.65—half model.

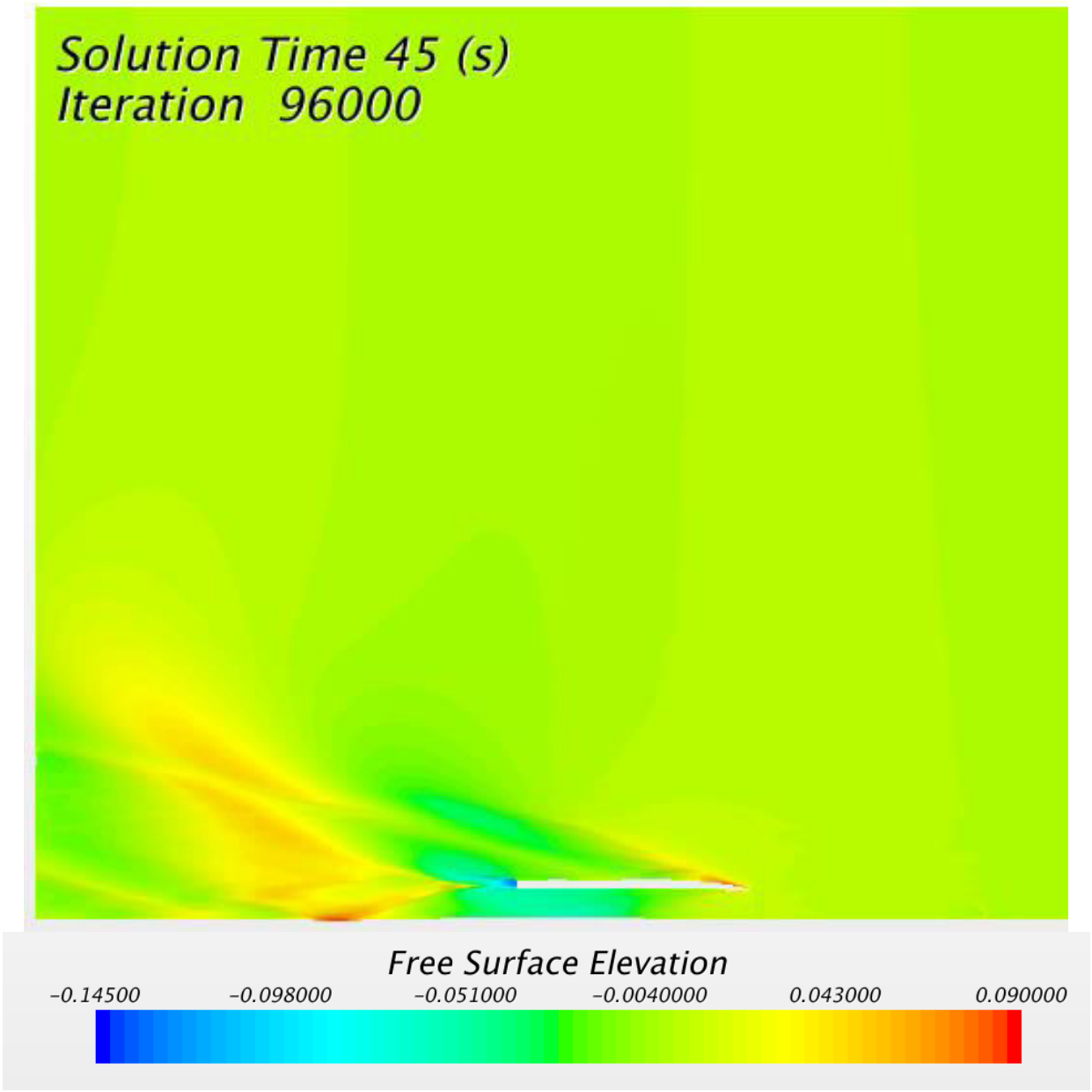

Figure 19: Free surface elevation contours scene of Fn_d=0.75—half model.

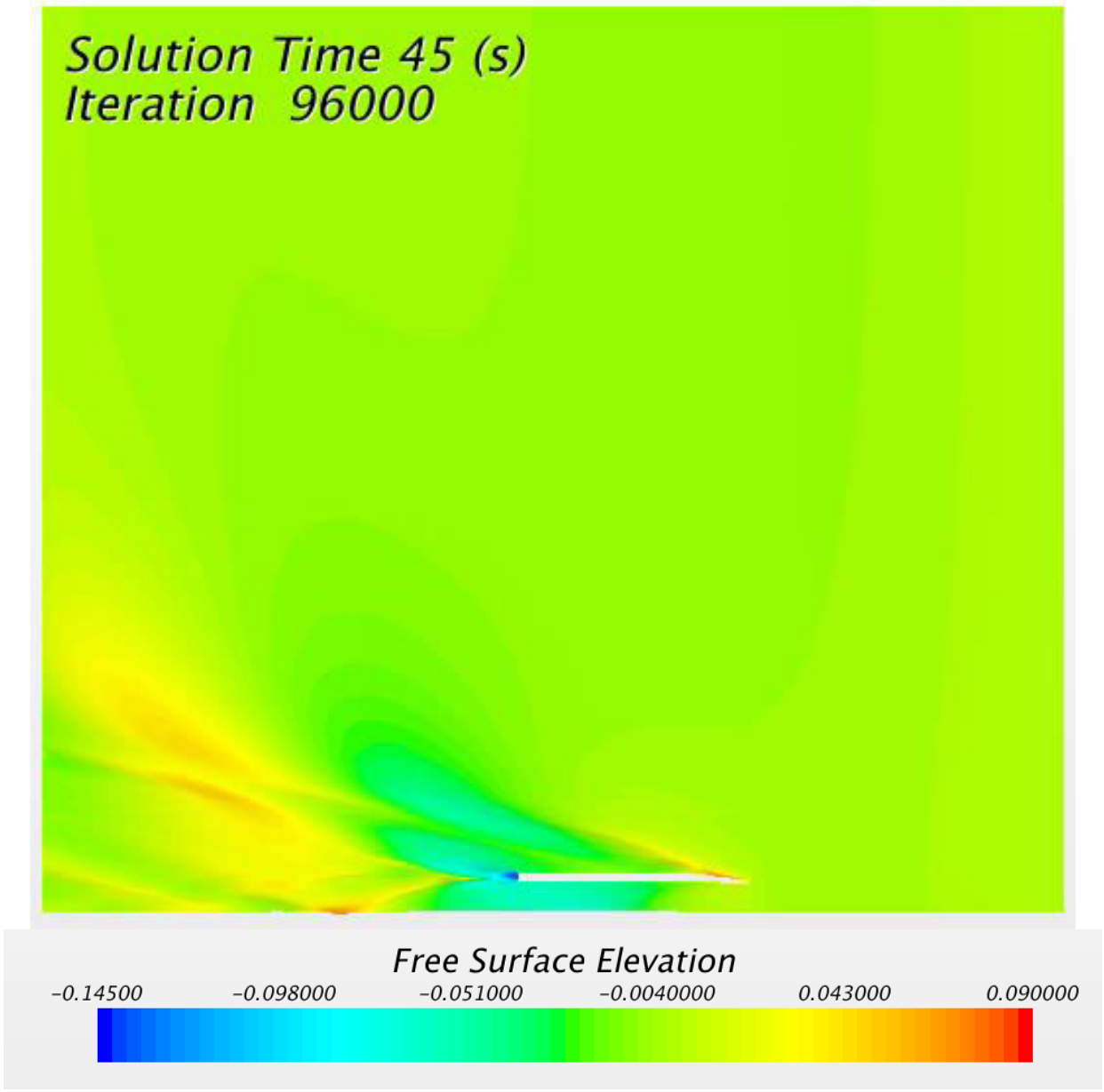

Figure 20: Free surface elevation contours scene of Fn_d=0.85—half model.

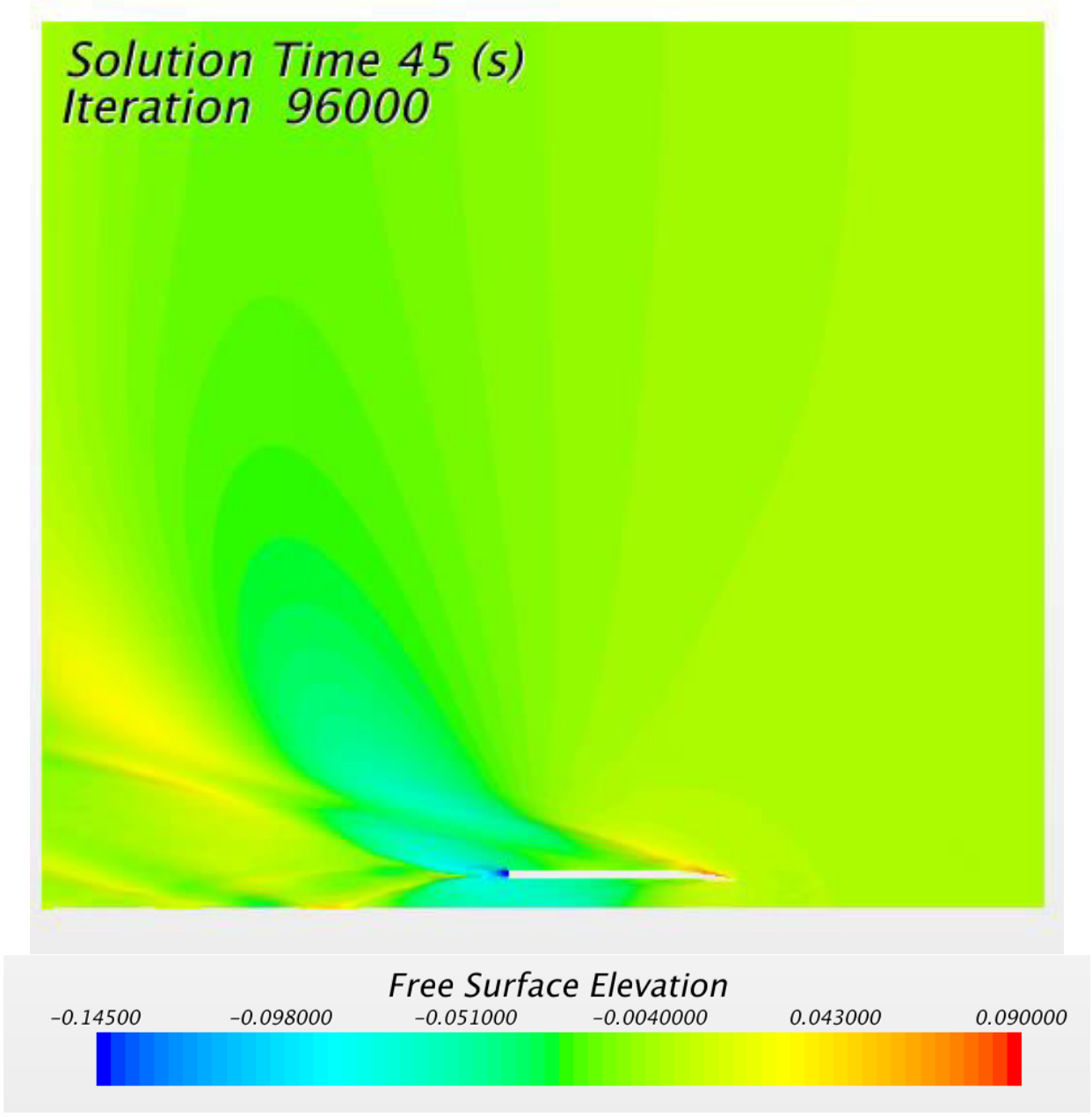

Figure 21: Free surface elevation contours scene of Fn_d=0.9—half model.

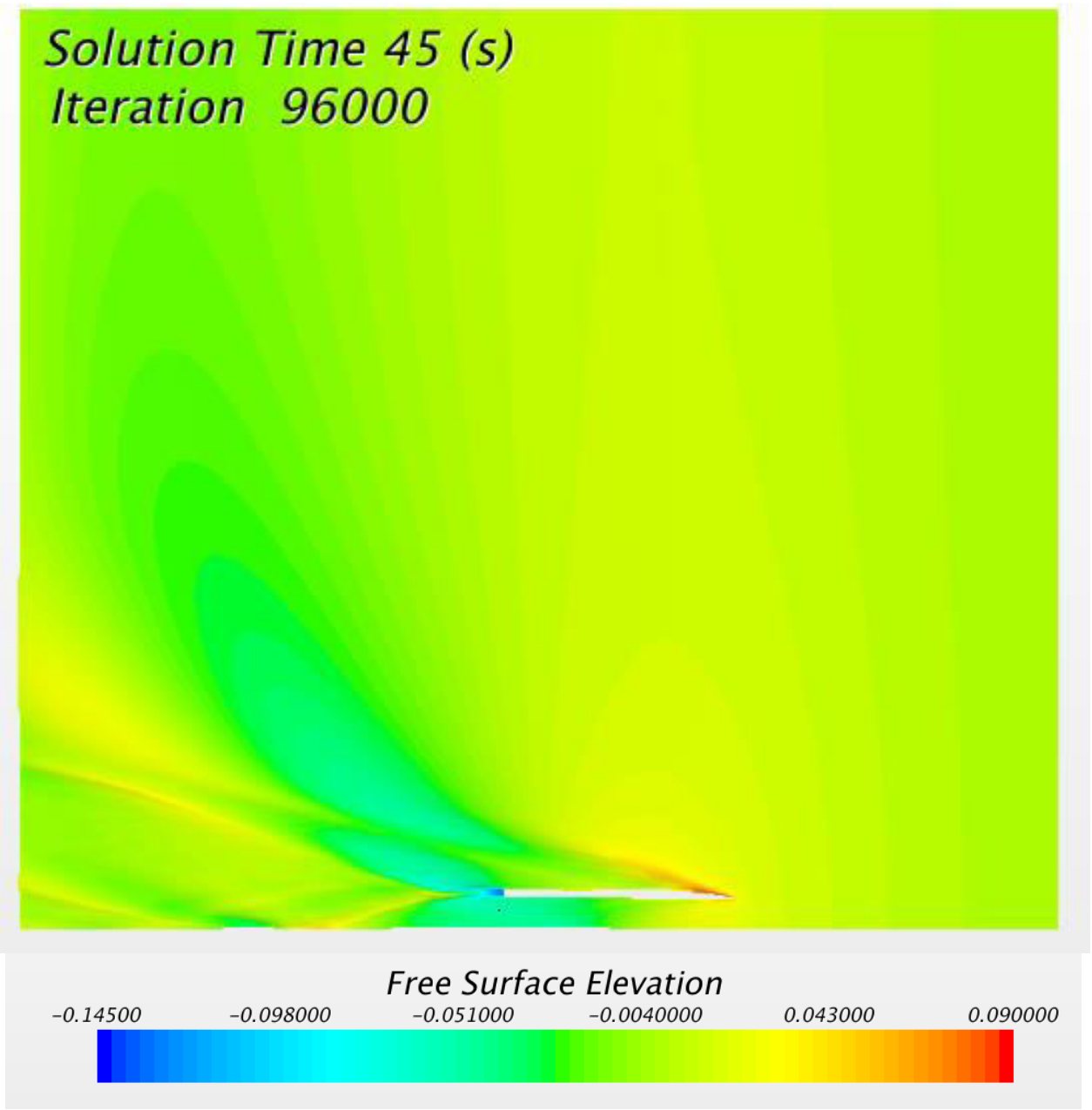

Figure 22: Free surface elevation contours scene of Fn_d=0.95—half model.

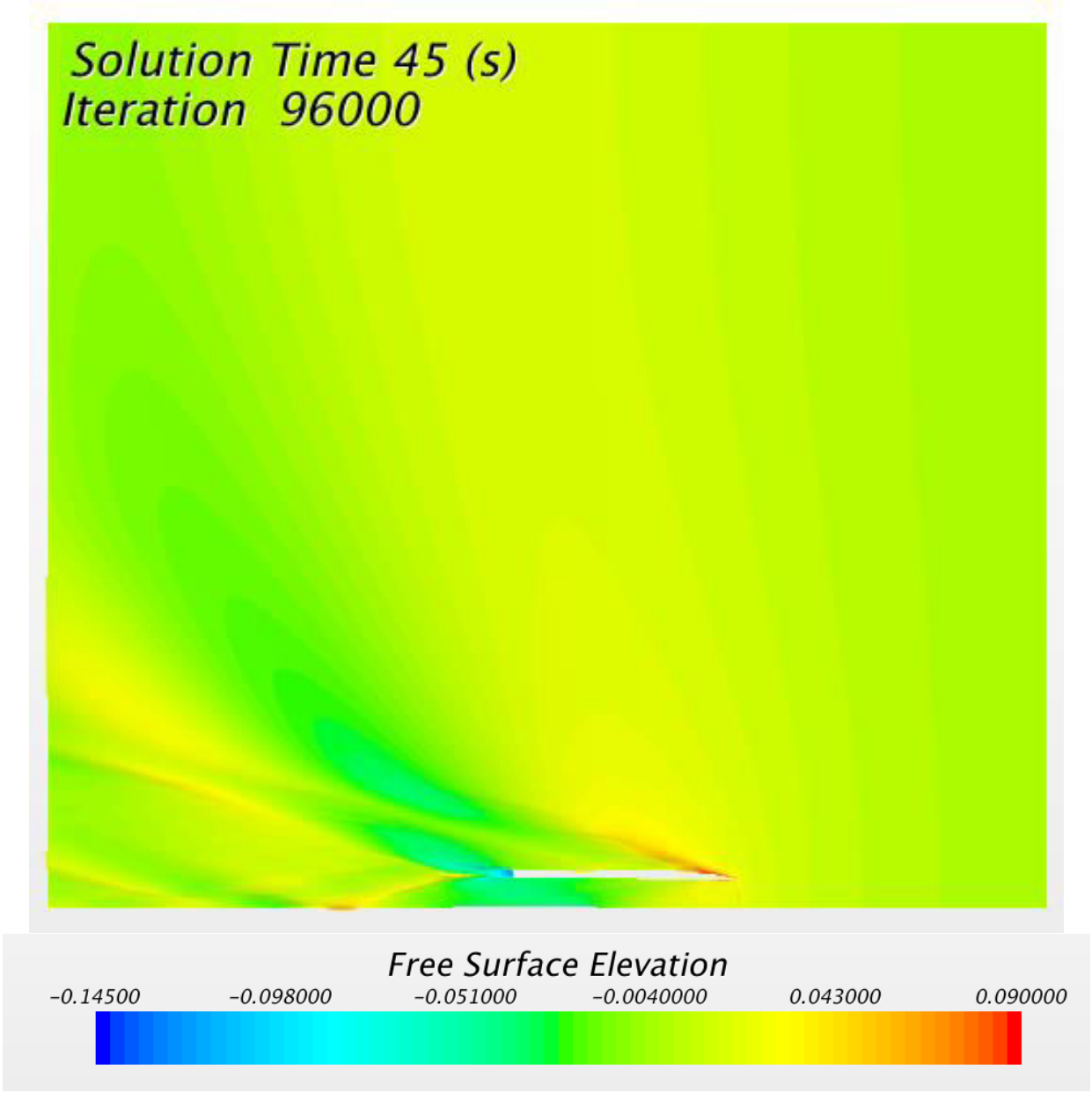

Figure 23: Free surface elevation contours scene of Fn_d=1.0—half model.

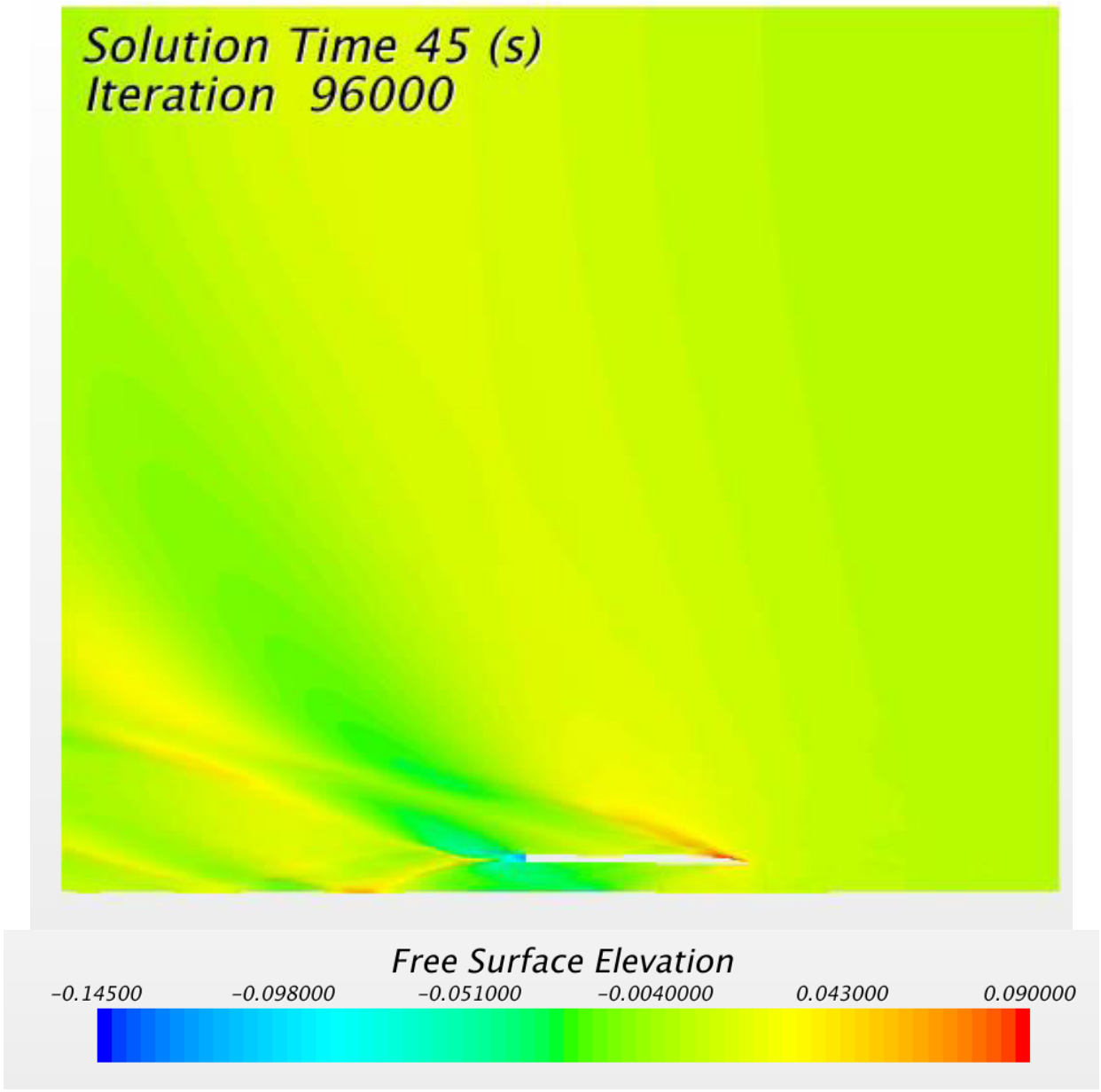

Figure 24: Free surface elevation contours scene of Fn_d=1.05—half model.

5.4 RESISTANCE AND PITCH RESULTS OF VARYING DEPTH SIMULATIONS

Monitoring the progression of the pitching motions of the craft as the depth Froude number increases offers a deeper understanding of the shallow water phenomena. Figure 25 is a plot of the one-second moving average of the steady state pitch over the last six seconds of simulation time for various depth Froude numbers. As previously stated, negative pitch is a bow up condition for the SES. Decreasing water depth leads to an increase in pitch until the critical change is reached at the depth Froude number of 0.9. Due to the limit of energy propagation imposed by the reduction of water depth, the SES begins to pitch back downwards once the supercritical speeds are reached. This behavior is reflected in Figure 25 when a depth Froude number greater than or equal to 0.95 is reached. The progression of pitch with increasing depth Froude number can be clearly seen in Figure 26. Pitch of the SES directly affects the induced wave making drag felt by the craft.

The plot of the one-second moving average of steady state drag for varying depth Froude numbers over the last six seconds of simulation time is seen in Figure 27. The drag is normalized by the weight of the SES. It can be seen that there is not much variation in steady state drag over the last six seconds of simulation time. Standard deviation error bars of the normalized drag are plotted for each depth Froude number. For depth Froude numbers 0.65-1.0, the standard deviation is within two percent of the mean. Two percent is a significant value because it is on the same magnitude as the cell size, 2 cm, of the volumetric control used to mesh the waterline. Standard deviation of the depth Froude number equal to 1.05 is just under three percent of the average drag. This increased unsteadiness is most likely due to greater non-dispersive effects present within the shallowest depth simulation. As previously stated, there is little decay of wake amplitude generated by the SES in the lateral direction. The wave system created by the bow of the SES extends to the spanwise domain boundary as seen in Figure 24. A larger spanwise domain size should be considered for these supercritical simulations. Normalized drag values, in Figure 27, follow the same trend as the pitch in Figure 25. The normalized drag increases with an increasing depth Froude number until the critical depth Froude number of 0.9 is reached. Once in the supercritical region, the resistance decreases with increasing depth Froude numbers. This progression of drag can be clearly seen in Figure 28. When comparing Figure 26 and Figure 28, it can be seen that the average pitch and average drag have an identical trend. Pitching of the SES directly affects the resistance. As the SES pitches upward, a larger component of the pressure cushion resists forward motion of the craft.

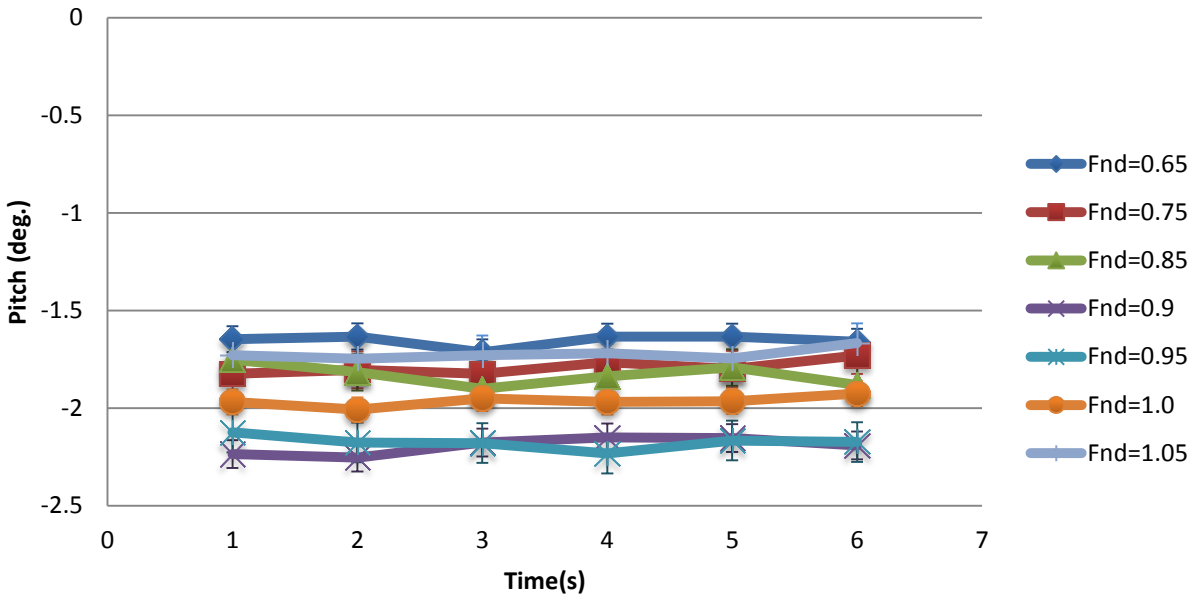

Figure 25: One-second moving average of steady-state pitch over the last 6 seconds of simulation time for various depth Froude numbers.

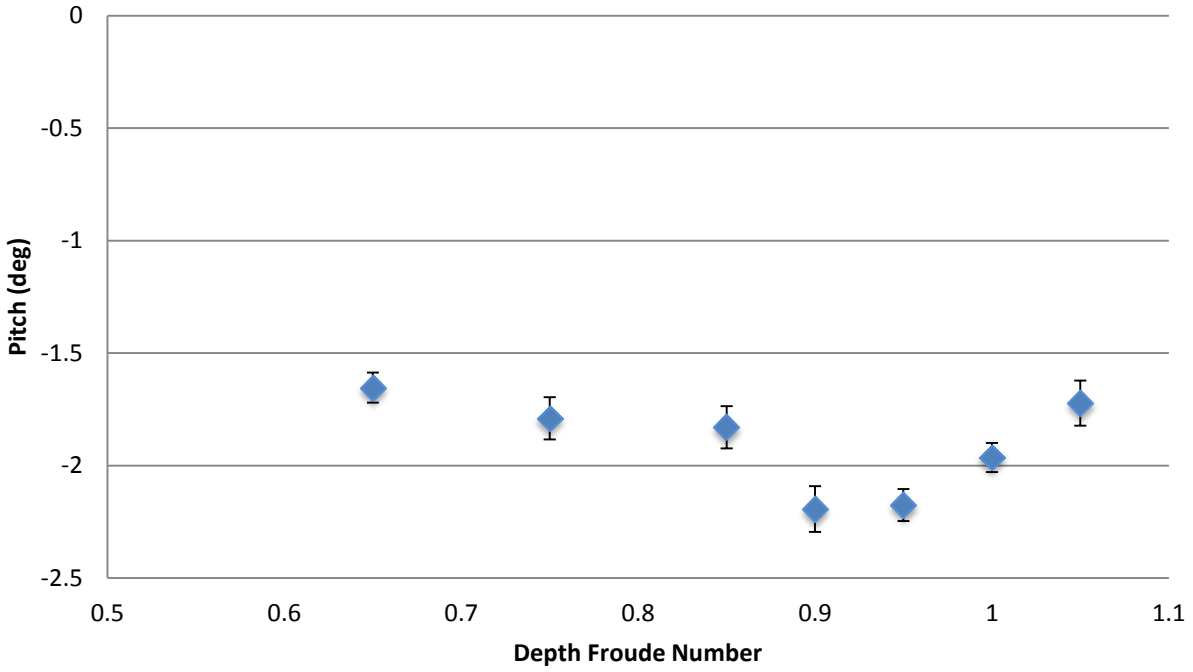

Figure 26: Progression of average pitch with an increasing depth Froude number.

5.5 SHALLOW WATER RESISTANCE CURVE OF CONSTANT DOMAIN DEPTH

All of the aforementioned shallow water simulations had a varying domain depth with a common incoming velocity, corresponding to a length Froude number equal to 0.6. Three simulations were created with the constant domain depth of approximately 0.98 meters. This correlates to $\frac{h}{L_c}$, where h is water depth and L_c is the cushion length of SES, equal to 0.44. The $\frac{h}{L_c}$ chosen was only for convenience since a critical depth Froude number simulation had already been produced. The incoming velocity was altered in each simulation to give subcritical, critical, and supercritical flow regimes. Resistance effects due to these changes in flow regimes for $\frac{h}{L_c}$=0.44 are presented by the resistance curve in Figure 29 and free surface elevation scenes in Figures 30-32. The transition from a lower subcritical drag, then to the peak drag, and back down to a lower supercritical drag can easily be seen in Figure 29. This transition matches nicely with the theoretical shallow water effects presented in Lewis [4]. The peak in Figure 29 occurs at a length Froude number, $\frac{V}{\sqrt{gL_c}} = 0.6$. Since $\sqrt{\frac{h}{L_c}} = 0.44$, this corresponds to a value of 0.9 for $\frac{V}{\sqrt{gh}}$. As previously shown, this is the critical speed for this particular depth. Standard deviation error bars are also plotted in Figure 29. The standard deviation of the normalized average drag increases with increasing length Froude number. The subcritical and critical simulations both contain a standard deviation within 2 percent of the steady state average drag. The supercritical simulation has a standard deviation that is 3.4 percent of the steady state average drag. This is the highest standard deviation present in any of the simulations. This higher unsteadiness is a function of both the shallow water and the increasing incoming velocity. The increase in unsteadiness of the simulations may also be contributed to the increase in velocity. A length Froude number of 0.8, corresponding to a depth Froude number of 1.2, was chosen to identify flow behavior at an even higher supercritical speed than analyzed by the previous shallow water simulations.

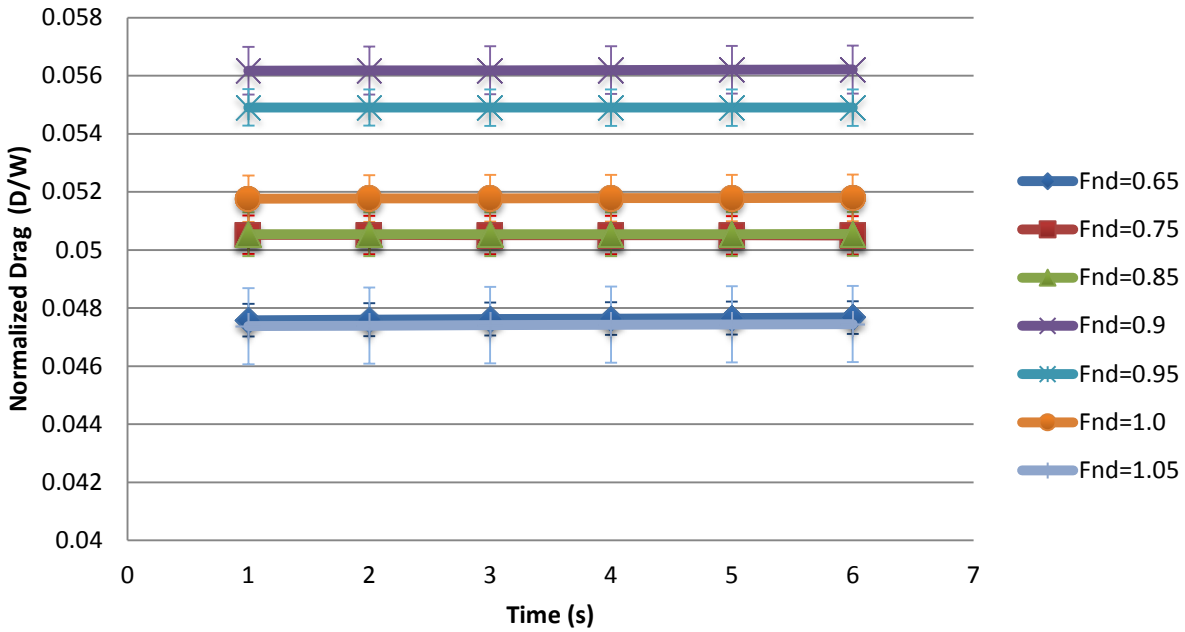

Figure 27: One-second moving average of steady-state drag over the last 6 seconds of simulation time for various depth Froude numbers.

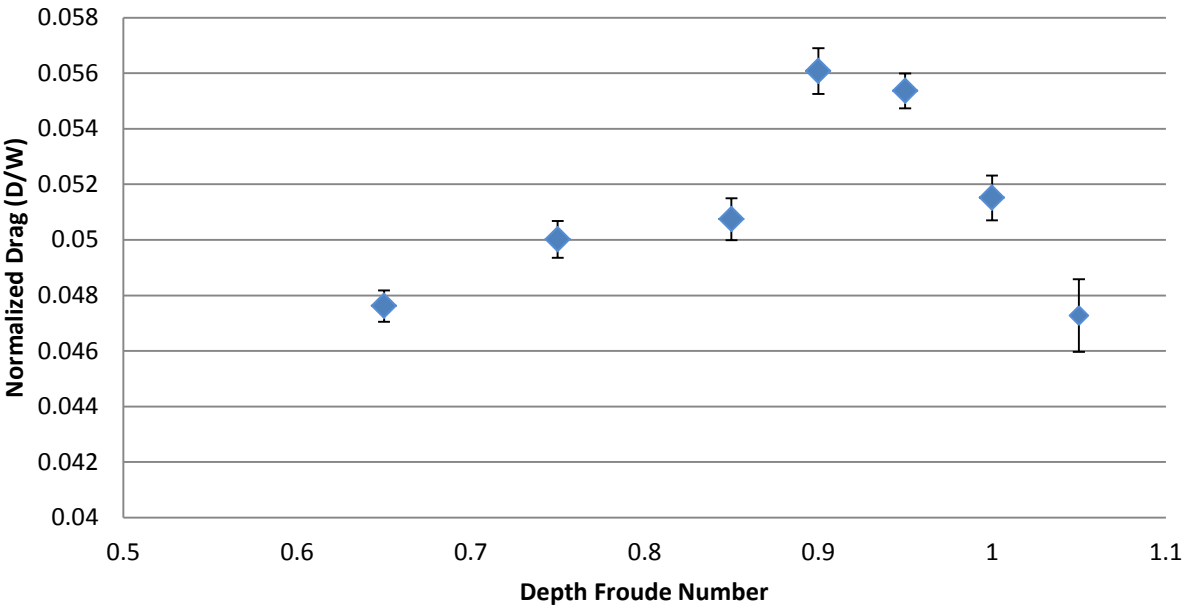

Figure 28: Progression of average normalized drag with an increasing depth Froude number.

5.6 FREE SURFACE ELEVATION CONTOURS OF CONSTANT DEPTH SHALLOW WATER SIMULATIONS

Figures 30-32 show the development of the wake as the length Froude number is increased from the subcritical through the supercritical regime. There are effects present from the shallow water and the changes in speed. As previously stated, the wake will grow in the span-wise direction until the critical depth Froude number is reached. Once in the supercritical regime, the wake narrows. Wave patterns generally consist of transverse and diverging waves. Both of these wave systems are easily distinguishable in Figure 30 and Figure 31. However, the supercritical regime, Figure 32, consists only of diverging waves. This was not as evident in the previously discussed supercritical flow regimes of the varying depth simulations.

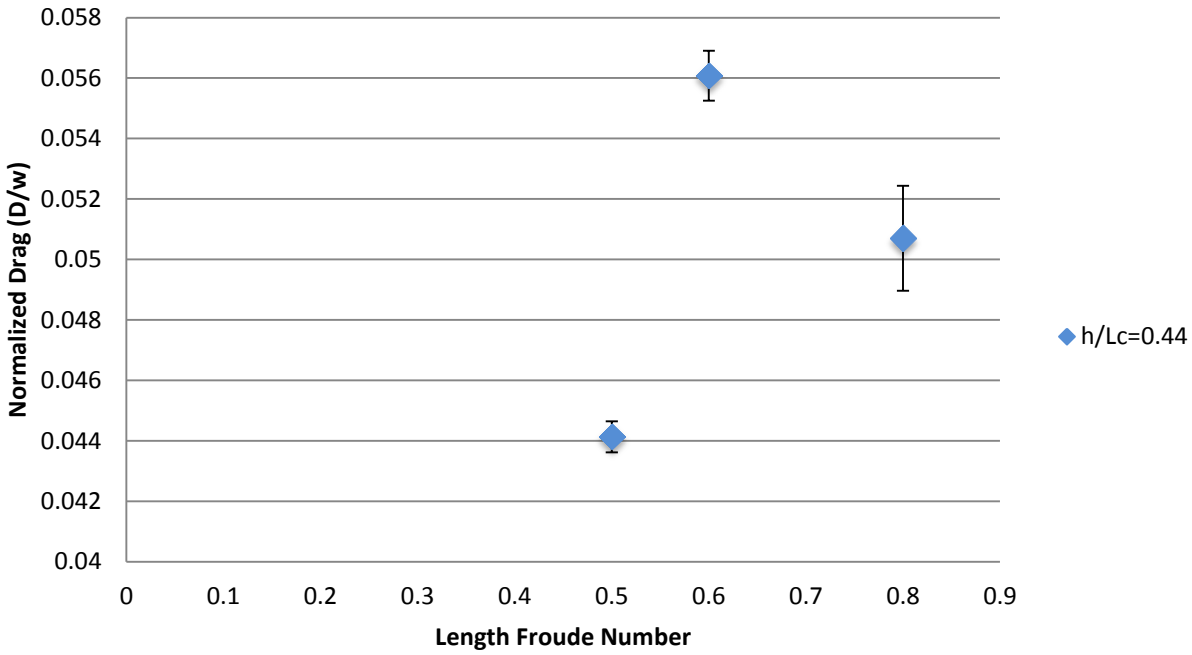

Figure 29: SES normalized drag through subcritical, critical and supercritical flow regimes.

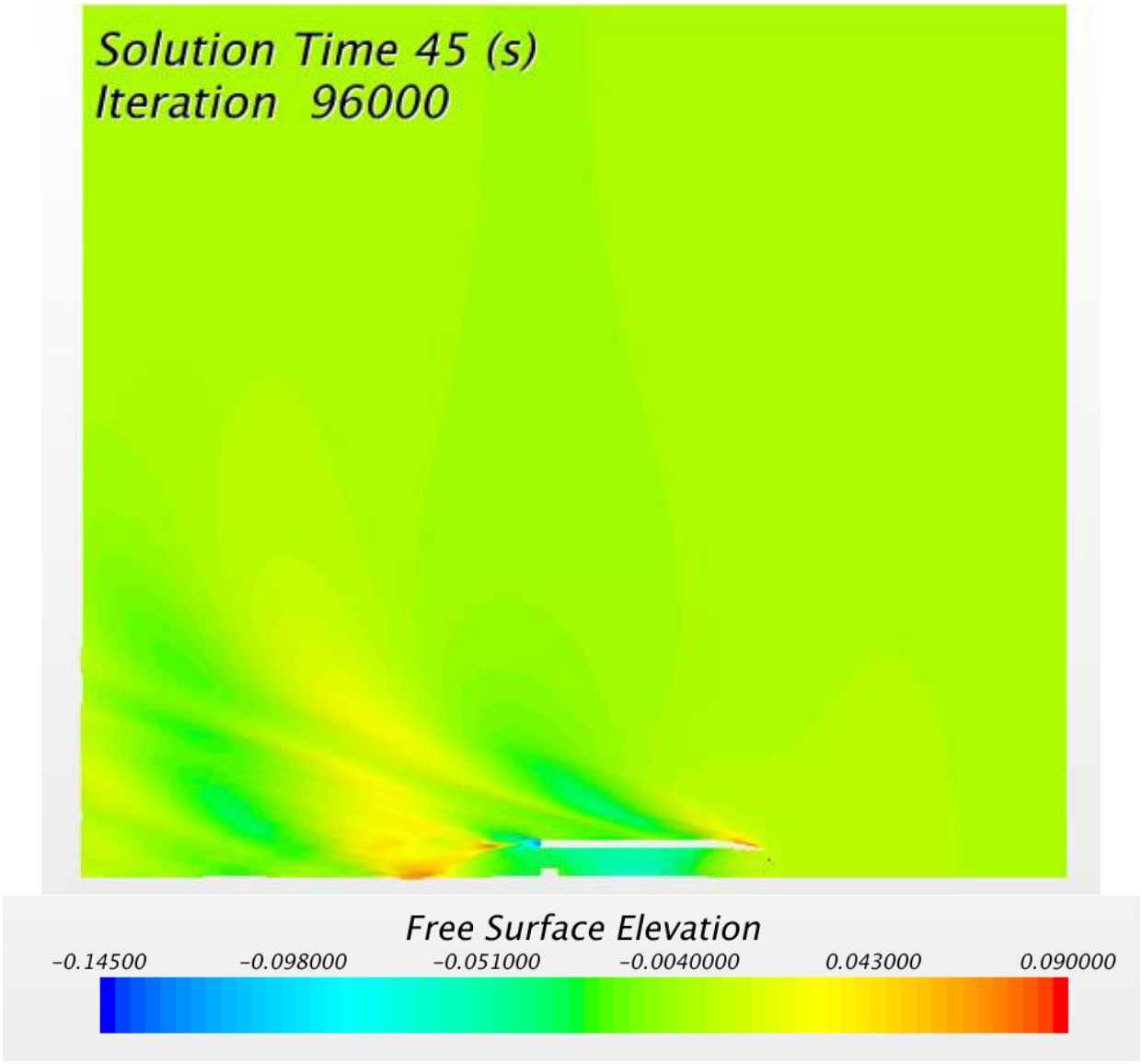

Figure 30: Free surface elevation contours scene of length Froude number equal to 0.5, corresponds to a depth Froude number of 0.75—half model.

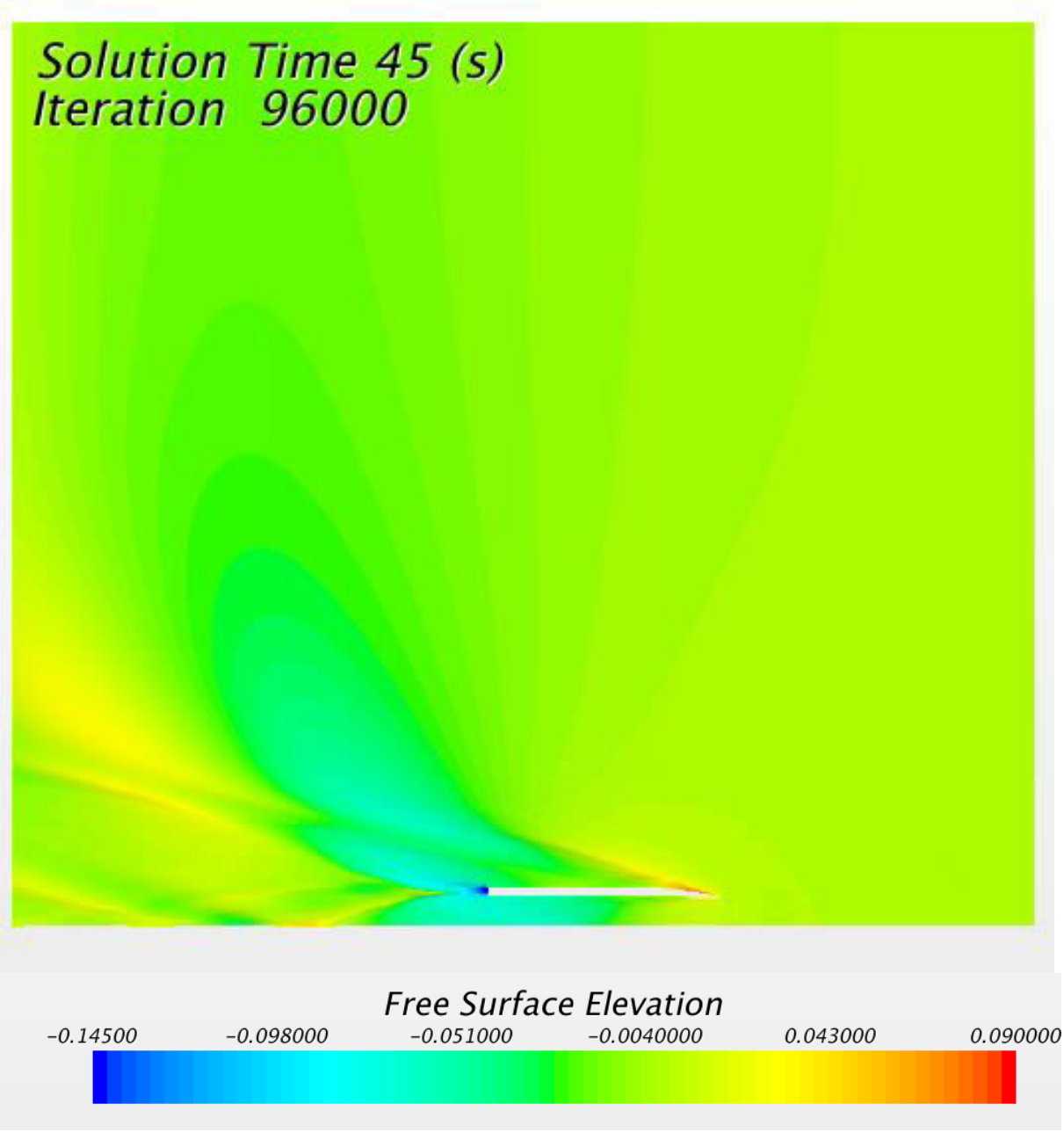

Figure 31: Free surface elevation contours scene of length Froude number equal to 0.6, corresponds to a depth Froude number of 0.9—half model.

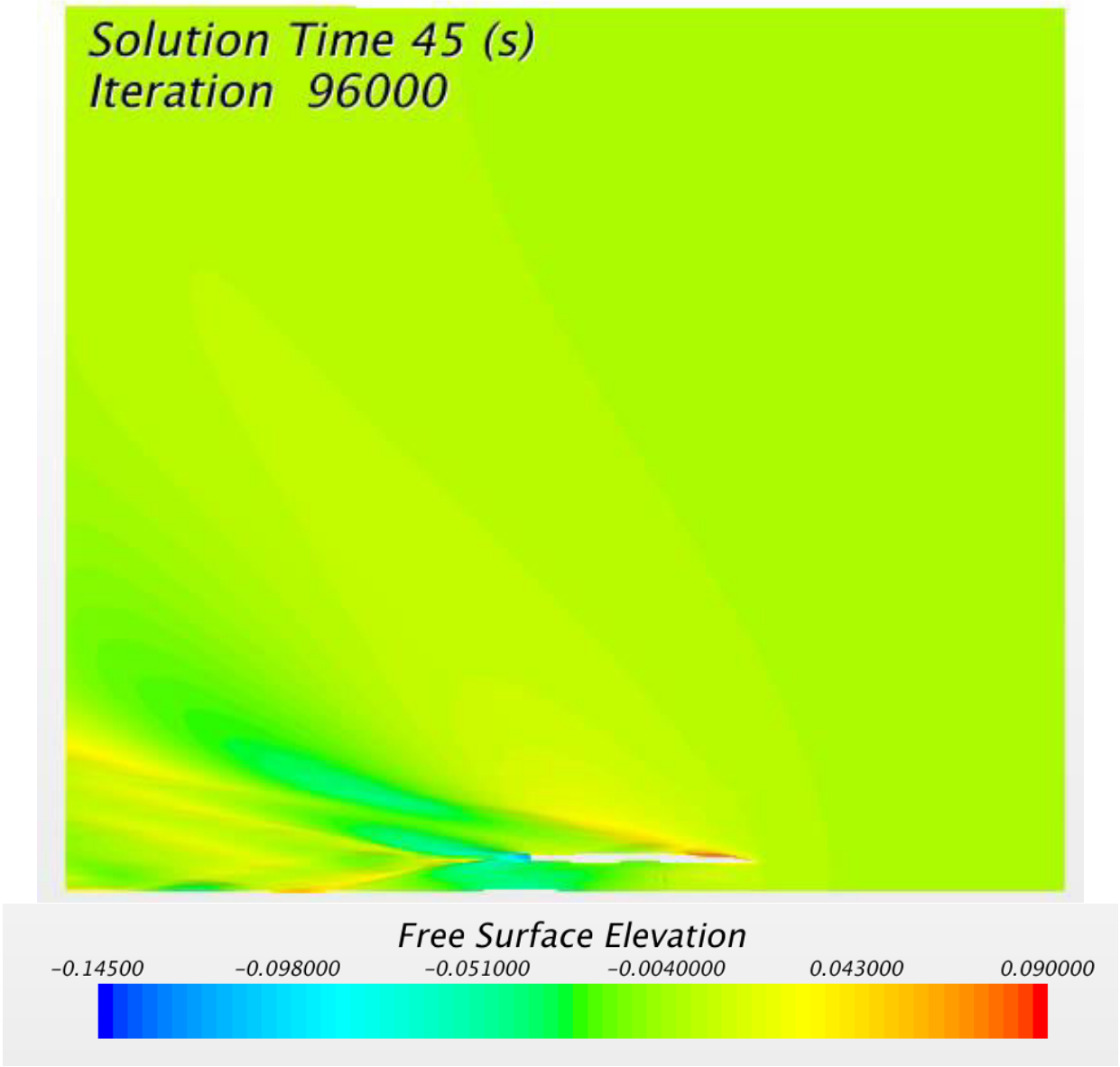

Figure 32: Free surface elevation contours scene of length Froude number equal to 0.8, corresponds to a depth Froude number of 1.2—half model.

6. CONCLUSIONS AND DISCUSSION

Numerical simulations of a SES hullform were performed using STAR-CCM+. Two meshing techniques were utilized for comparison, a traditional single grid approach and an overset multigrid approach. The first goal was to prove the resistance results between the two grids corresponded. Once correspondence was proven, the overset, multigrid, approach could be implemented to analyze shallow water cases. The overset grid approach has many advantages. One major advantage is that it allows for relative motion between two objects without remeshing between time steps or skewed cells. However, the less efficient CPU times of the overset grid deem it unsuitable for application unless it is completely necessary.

Shallow water simulations require the use of an overset grid for relative motion between the hullform and the domain bottom. Observing the free surface elevation contours shows the trend in wake pattern as the SES moves through subcritical, critical, and supercritical flow regimes. Transverse waves disappear as larger depth Froude numbers in the supercritical regime are approached. The wider waked and non-dispersive natured shallow water simulations necessitate a larger span-wise domain size than deep water simulations to help mitigate the unsteadiness of the solution. Unsteadiness in the shallow water simulations increases as the water depth decreases. This is most likely due to the interaction of the bow and stern wave systems with the spanwise domain boundary. Another source of unsteadiness can be attributed to the rigid skirt approximation of the SES. The need for a dynamic flexible seal in the simulations cannot be overstated.

The critical depth Froude number for the T-Craft measured in the numerical simulations falls below the theoretical critical depth Froude number of unity because of its smaller length to beam ratio and cushion pressure. Determining the location of the critical depth Froude number gives insight to appropriate operating zones for the SES in shallow water. Future work would be extended to show the effect of a SES accelerating through the critical depth Froude number.

7. REFERENCES

[1] Donnelly, D., “Numerical Simulation of Surface Effect Ship Air Cushion and Free Surface Interaction,” M.S. Thesis, Virginia Tech, 2010.

[2], R. C., Silver, A. L., Tahmasian, D., Lee, S. S., Park, J. T, Snyder, L. A., and Kim, J. 2009. “T-Craft seabase Seakeeping Model Test Data Report,” NSWCCD-50-TR–2009/055, Hydro-mechanics Department Report.

[3] Yun, L. and Bliault, A. *Theory and Design of Air Cushion Craft,* 2000, L. Yun and A. Bliault, Bath Press, Great Britain.

[4] Lewis, Edward V., *Principles of Naval Architecture*, Vol. II, 1988. Society of Naval Architects and Marine Engineers, Jersey City, NJ, USA.

[5] Newman, J. N., *Marine Hydrodynamics*, 1977. MIT Press, Cambridge, MA.

[6] Hirt, C.W. and Nichols, B.D.,”Volume of Fluid (VOF) Method for Dynamics of Free Boundaries,” *Journal of Computational Physics*, Vol. 39, pp. 201-225, 1981.

[7] CD-Adapco/STAR-CCM+8.02.011/help guide.

[8] Hadzic, H., “Development and Application of Finite Volume Method for the Computation of Flows Around Moving Bodies on Unstructured, Overlapping Grids’” PhD thesis, Technical University Hamburg-Harburg, 2005.

[9] Clark, C., Lyons, D., and Neu, W. L., “Comparison of Single and Overset Grid Techniques for CFD Simulations of a Surface Effect Ship,” in Proceedings of the ASME 2014 33rd International Conference on Ocean, Offshore and Arctic Engineering, San Francisco, CA, 2014.

[10] T. Xing and F. Stern, "Factors of Safety for Richardson Extrapolation," Journal of Fluids Engineering, vol. 132, p. 061403, 2010.

[11] Donnelly, D. J. and W. L. Neu, “Numerical Simulation of Flow About a Surface-Effect Ship,” Proceedings 11th International Conference on Fast Sea Transportation, FAST 2011, Honolulu, Hawaii, USA, September 26-29, 2011.

[12] Kramer, M. R., and Wilson, R. A., “Implications of Water Depth on Surface Effect Ship Operations,” Fulcrum Corporation, 2009.

[13] Newman J.N., and F. A. Poole, "The Wave Resistance of a Moving Pressure Distribution in a Canal," DRNSRDC Report 1619, Mar. 1962.

[14] Doctors, L.J., "The Wave Resistance of an Air Cushion Vehicle," University of Michigan, Dec. 1970.

[15] Bhushan, S., Stern, F., and Doctors, L.J., "Verification and Validation of URANS Wave Resistance for Air Cushion Vehicles, and Comparison With Linear Theory," *Journal of Ship Research,* Vol. 55, pp. 249-267, 2011.

[16] Faltinsen, Odd M. *Hydrodynamics of High-Speed Marine Vehicles,* 2005. Cambridge University Press, New York, NY, USA.